JGR Space Physics

RESEARCH ARTICLE
10.1029/2023JA032179

Key Points:

- Most intense H-band electromagnetic ion cyclotron (EMIC) wave packets are short but 3%–10% may lead to nonlinear interactions
- The power spectrum of intense H-band EMIC wave packets contains a significant high-frequency tail
- Resonant interactions with intense H-band EMIC wave packets likely play an important role in sub-relativistic electron precipitation

Correspondence to:
X. Shi,
sxf1698@g.ucla.edu

Citation:
Shi, X., Artemyev, A., Zhang, X.-J., Mourenas, D., An, X., & Angelopoulos, V. (2024). Properties of intense H-band electromagnetic ion cyclotron waves: Implications for quasi-linear, nonlinear, and nonresonant wave-particle interactions. *Journal of Geophysical Research: Space Physics*, *129*, e2023JA032179. https://doi.org/10.1029/2023JA032179

Received 15 OCT 2023
Accepted 21 DEC 2023

Properties of Intense H-Band Electromagnetic Ion Cyclotron Waves: Implications for Quasi-Linear, Nonlinear, and Nonresonant Wave-Particle Interactions

Xiaofei Shi[1], Anton Artemyev[1], Xiao-Jia Zhang[1,2], Didier Mourenas[3,4], Xin An[1], and Vassilis Angelopoulos[1]

[1]Department of Earth, Planetary, and Space Sciences, University of California, Los Angeles, CA, USA, [2]Department of Physics, University of Texas at Dallas, Richardson, TX, USA, [3]CEA, DAM, DIF, Arpajon, France, [4]Laboratoire Matière en Conditions Extrêmes, Université Paris-Saclay, CEA, Bruyères-le-Châtel, France

Abstract Resonant interactions between relativistic electrons and electromagnetic ion cyclotron (EMIC) waves provide an effective loss mechanism for this important electron population in the outer radiation belt. The diffusive regime of electron scattering and loss has been well incorporated into radiation belt models within the framework of the quasi-linear diffusion theory, whereas the nonlinear regime has been mostly studied with test particle simulations. There is also a less investigated, nonresonant regime of electron scattering by EMIC waves. All three regimes should be present, depending on the EMIC waves and ambient plasma properties, but the occurrence rates of these regimes have not been previously quantified. This study provides a statistical investigation of the most important EMIC wave-packet characteristics for the diffusive, nonlinear, and nonresonant regimes of electron scattering. We utilize 3 years of observations to derive distributions of wave amplitudes, wave-packet sizes, and rates of frequency variations within individual wave-packets. We demonstrate that EMIC waves typically propagate as wave-packets with ∼10 wave periods each, and that ∼3–10% of such wave-packets can reach the regime of nonlinear resonant interaction with 2–6 MeV electrons. We show that EMIC frequency variations within wave-packets reach 50–100% of the center frequency, corresponding to a significant high-frequency tail in their wave power spectrum. We explore the consequences of these wave-packet characteristics for high and low energy electron precipitation by H-band EMIC waves and for the relative importance of quasi-linear and nonlinear regimes of wave-particle interactions.

1. Introduction

Electromagnetic ion cyclotron (EMIC) waves are one of the main waves controlling the dynamics of relativistic electron fluxes via resonant wave-particle interactions (see reviewers by Millan & Thorne, 2007; Shprits et al., 2008; Usanova, 2021, and references therein). These waves are generated by hot ion distributions with temperature anisotropy (Sagdeev & Shafranov, 1961; Thorne & Kennel, 1971) that are either injected from the night-side plasma sheet or heated by day-side magnetosphere compressions (see EMIC waves statistics in Usanova et al., 2012; Zhang et al., 2016; Jun et al., 2019, 2021).

1.1. Quasi-Linear Electron Resonant Interaction With EMIC Waves

The classical and most widespread treatment of electron scattering by EMIC waves is quasi-linear diffusion through cyclotron resonance, which depends on the time-averaged wave power as a function of the wave frequency normalized to the proton gyrofrequency (e.g., Albert, 2003; Drozdov et al., 2017; Kersten et al., 2014; Ni et al., 2015; Ross et al., 2020; Shprits et al., 2016; Summers & Thorne, 2003; Thorne & Kennel, 1971). However, this approach may not be sufficient to explain observations of sub-relativistic electron precipitation below ∼0.5 MeV during conjunctions with EMIC wave bursts near the equator (X. An, Artemyev, et al., 2022; Angelopoulos et al., 2023; Capannolo, Li, Ma, Shen, et al., 2019; Hendry et al., 2017), because the frequency of the most intense observed EMIC waves is usually not sufficiently high to reach cyclotron resonance with sub-relativistic electrons (Kersten et al., 2014; Ni et al., 2015). Moreover, the quasi-linear approach cannot describe a potentially important regime of wave-particle interactions: nonlinear resonant interactions (see examples in Albert & Bortnik, 2009; Grach & Demekhov, 2018a, 2018b; Omura & Zhao, 2012, 2013).

1.2. Nonlinear Electron Resonant Interaction With EMIC Waves

EMIC wave amplitudes often exceed hundreds of pT (Meredith et al., 2014; Zhang et al., 2016) and are large enough to reach the regime of nonlinear resonant interaction, when the wave Lorentz force exceeds the electron mirror force in an inhomogeneous magnetic field, and thus significantly changes electron trajectories (see details of the basic concept of nonlinear resonant interaction in reviews by Albert et al., 2013; Artemyev et al., 2018; Shklyar & Matsumoto, 2009; Omura et al., 1991). Such a significant effect on electron dynamics breaks the key assumption of the quasi-linear theory which is the approximation of unperturbed particle trajectories and requires consideration of more sophisticated effects than diffusive scattering (Albert & Bortnik, 2009). Quite comprehensive parametric investigations of possible nonlinear resonant effects for electron interactions with EMIC waves can be found in Kubota et al. (2015), Kubota and Omura (2017), Grach and Demekhov (2020), Hanzelka, Li, and Ma (2023). Here, we discuss the two most important nonlinear processes: phase bunching and phase trapping.

Electron phase bunching is a nonlinear resonant effect occurring when the wavefield is sufficiently strong to keep electrons in resonance with the wave over a time scale of multiple gyroperiods, that may change their pitch-angle and energy. Such phase bunching by EMIC waves results in an increase in pitch-angle, and is not a diffusive process: an ensemble of electrons with the same energy and pitch-angle, but random gyrophases, will experience pitch-angle increase with a finite mean value (see examples in Albert & Bortnik, 2009; Grach & Demekhov, 2018b, 2020; Su et al., 2012). Such pitch-angle drift in phase space moves electrons away from the loss cone and can potentially reduce the efficiency of electron precipitation (see discussion in Bortnik et al., 2022). The pitch-angle change due to a single resonant interaction (during one bounce period) scales with the normalized amplitude B_w/B_0 of EMIC waves as $\Delta\alpha \propto \sqrt{B_w/B_0}$ (e.g., Albert & Bortnik, 2009, and references therein), and is larger than the drift due to diffusion $\Delta\alpha \propto (B_w/B_0)^2$ (see discussion in Bortnik et al., 2022). Phase bunching is a local process and only depends on wave amplitude at the resonance. Therefore, the important EMIC wave characteristic that is required to quantify this process is the range of variation of instantaneous wave intensity. Note that the existing EMIC wave data sets (Meredith et al., 2014; Ross et al., 2021; Zhang et al., 2016) provide only time-averaged wave power from Fourier analysis of EMIC spectra which, for short wave-packets, can lead to a significant underestimation of the instantaneous peak wave intensity.

Electron phase trapping is a nonlinear resonant effect occurring when the wavefield can lock electrons around the resonance on a time-scale of a fraction of the electron bounce period, that may change their pitch-angle and energy. Such phase trapping by EMIC waves results in a decrease in pitch-angle, and constitutes one of the main mechanisms responsible for fast electron precipitation by intense EMIC waves (Grach et al., 2021; Hanzelka, Li, & Ma, 2023; Kubota & Omura, 2017). Such trapping is nonlocal, that is, the efficiency of the associated electron transport in pitch-angle and energy depends on the shape/size of EMIC wave-packets and their coherence (see discussion of this effect for various waves types in Z. An, Artemyev, et al., 2022; Grach & Demekhov, 2020; Mourenas et al., 2018; Tao et al., 2013; Zhang, Agapitov, et al., 2020). Therefore, for an accurate quantification of phase trapping we need information on the fine structure of EMIC wave-packets, including wave-packet size, wave phase, and frequency variations that may terminate phase trapping.

1.3. Nonresonant Electron Interaction With EMIC Waves

In contrast to the nonlinear resonant interaction, which is responsible for rapid electron flux variations, nonresonant effects (Chen et al., 2016) are relatively weak, second-order effects. However, these nonresonant effects can play a crucial role in the precipitation of sub-relativistic electrons. Such sub-relativistic precipitation associated with EMIC waves has been frequently observed (e.g., Angelopoulos et al., 2023; Capannolo, Li, Ma, Chen, et al., 2019). However, it cannot be described by resonant interactions with the most intense observed EMIC waves, because such resonant interactions are often limited to energies above 1 MeV, due to the insufficiently high frequency of the main waves (e.g., Kersten et al., 2014; Ni et al., 2015; Ross et al., 2021). Although some part of the sub-relativistic precipitation could perhaps be explained by hot plasma effects on the EMIC wave dispersion (Bashir et al., 2022; Silin et al., 2011), such hot plasma effects usually tend to increase the minimum resonant energy and cannot explain sub-relativistic precipitation (Cao et al., 2017; Chen et al., 2019). One well-known type of nonresonant electron scattering can be understood as curvature scattering (Artemyev et al., 2015; Birmingham, 1984; Buchner & Zelenyi, 1989; Chirikov, 1987; Delcourt et al., 1994), where the pitch-angle change is exponentially scaled with its difference in energy from the resonance energy (see general theory in Neishtadt, 2000). In the case of EMIC waves, the wave-packet size, or the wave amplitude modulation,

plays a crucial role in the determination of the wave number range (i.e., the range of spatial scales of magnetic field fluctuations) for the nonresonant interaction and, thus, controls the efficiency of this effect (X. An, Artemyev, et al., 2022, 2023; Chen et al., 2016).

Over a short spatial extent, an EMIC wave-packet can contain a broad spectrum of wavenumbers k distributed around the wavenumber of peak power, k_0. The upper range of this k spectrum allows cyclotron resonant interactions between subrelativistic electrons with waves of much smaller amplitude than the main waves, corresponding to the wavenumber k_0, which interact with higher energy electrons. Since EMIC wave frequencies ω are lower than the proton gyrofrequency Ω_{ci} and much lower than the electron gyrofrequency $\Omega_{ce} = 1{,}836\ \Omega_{ci}$, the cyclotron resonance condition for parallel EMIC waves can be rewritten as $kv/\Omega_{ce} = 1/(\gamma \cos \alpha)$, with γ the Lorentz factor, v and α the electron velocity and pitch-angle (Angelopoulos et al., 2023; Summers & Thorne, 2003). Consequently, any magnetic fluctuation of sufficiently low frequency, $\omega \ll \Omega_{ce}$, can resonantly scatter low energy electrons if its wave number k is sufficiently high to satisfy the above resonance condition (e.g., see Xu & Egedal, 2022). For typical high-k EMIC waves of low amplitudes (Denton et al., 2019), this resonant scattering is proportional to the wave power and much more efficient than purely nonresonant scattering (X. An, Artemyev, et al., 2022; Angelopoulos et al., 2023; Xu & Egedal, 2022). Therefore, the nonresonant electron interactions with EMIC waves could be more precisely recast as nonresonant with the main EMIC waves (at peak wave power) while still resonant with much lower intensity EMIC waves at higher wave numbers k, which usually correspond to higher ω/Ω_{ci} values based on the EMIC wave dispersion relation (Denton et al., 2019; Summers & Thorne, 2003). To quantify the effects of such sub-relativistic electron interactions with EMIC wave-packet edges, we need statistical information about EMIC wave-packet characteristics, such as the wave power spectrum tail at high ω/Ω_{ci}, which should correspond to high wave numbers k.

1.4. On the Most Significant Characteristics of EMIC Wave-Packets

Because of their importance for identifying the different regimes of wave-particle interactions, we statistically investigate the following EMIC wave-packet characteristics: wave-packet size, percentage of wave packets that can interact resonantly with electrons nonlinearly, and details of variations of wave frequency and wave power within wave-packets. We start with a description of the EMIC wave data set and the methods of wave-packet determination in Section 2. Then in Section 3 we describe statistical characteristics of wave-packet amplitudes and sizes, and in Section 4 we provide information about the inner structure of wave-packets. Section 5 examines the consequences of wave packet characteristics for the energy of precipitating electrons, and the relative importance of quasi-linear, nonlinear, and nonresonant wave-particle interactions. Finally, in Section 6 we summarize the results.

2. Instrumentation and Data Sets

The twin Van Allen Probes were launched on 2012-08-30 into a near-equatorial elliptical orbit with geocentric apogee 5.8 R_E and perigee 1.1 R_E (Mauk et al., 2013). High-resolution magnetic field data are obtained from the Electric and Magnetic Field Instrument Suite and Integrated Science (EMFISIS) fluxgate magnetometer (Kletzing et al., 2013). The plasma density is derived from the upper hybrid frequency measured by EMFISIS High-Frequency Receiver (Kurth et al., 2015) or can be calculated using spacecraft potential from the Electric Field and Waves instrument (Wygant et al., 2013).

In this study, we examined proton band EMIC wave events collected by Van Allen Probes from 2012 to 2015 (the EMIC wave data set is the same as in Zhang et al., 2016). To select wave packets in each event, we used two different criteria: (a) wave packets with peak amplitude $B_{w,\mathrm{peak}} > 0.2$ nT and dips in amplitude below 0.1 nT on each side of the peak; (b) wave packets with peak amplitude $B_w > 0.2$ nT and dips in amplitude below $0.5B_{w,\mathrm{peak}}$ on each side of the peak. Then we calculated the wave packet size (β) as the number of wave periods between two edges of each packet. The main difference between these two criteria is that when the wave amplitude is large, that is, $B_{w,\mathrm{peak}} > 0.5$ nT, the noticeable dips near the amplitude peak may not be smaller than 0.1 nT. Thus the first criterion will favor large packet sizes for intense waves. This bias is avoided by the second criterion in which the threshold for the amplitude dip is not fixed but varies with the peak amplitude, allowing detection of sub-packets when the waves are particularly intense. Figure 1 shows an observation of EMIC waves and the wave packets selected using the two above-described criteria. Note that the wave amplitude used to select the packet

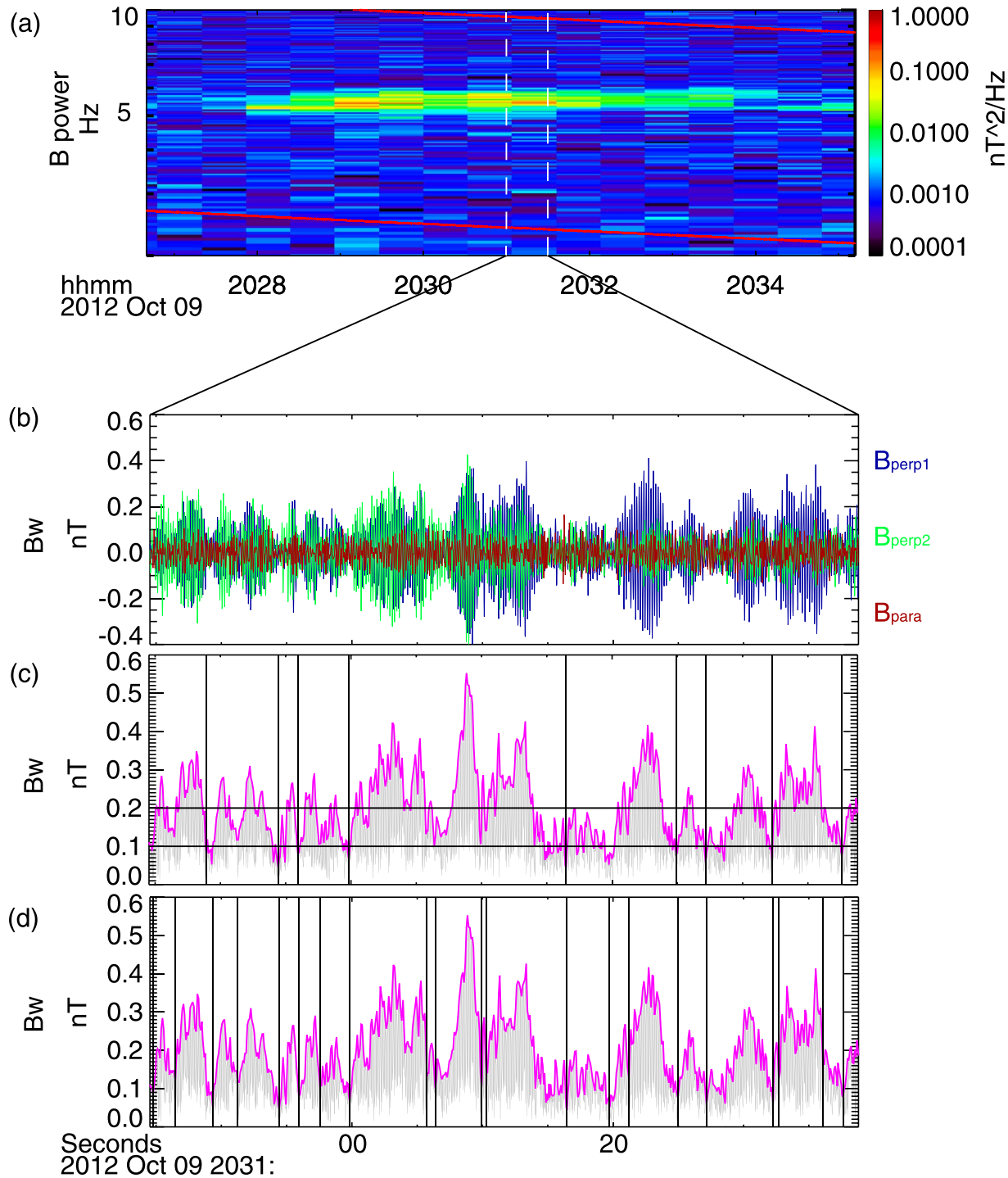

Figure 1. Observations of H-band electromagnetic ion cyclotron waves: (a) wave power spectrum. Two red lines from top to bottom indicate proton and helium cyclotron frequency, respectively; (b) two perpendicular components and the parallel component of wave magnetic field in field-aligned coordinate; (c) Wave amplitude and wave packets determined by criterion (1); (d) wave packets determined by criterion (2). The vertical black lines in Panels (c) and (d) show the edge of wave-packets.

is the envelope of the full wave amplitude (the magenta lines in Figures 1c and 1d). A similar observation of H-band EMIC waves, but this time simultaneously recorded by two spacecraft of the Time History of Events and Macroscale Interactions during Substorms (THEMIS) mission (Angelopoulos et al., 2008), using magnetic field measurements with 1/5 s sampling rate (fgl data set) from the Fluxgate magnetometer (Auster et al., 2008), will be examined in the Discussion section.

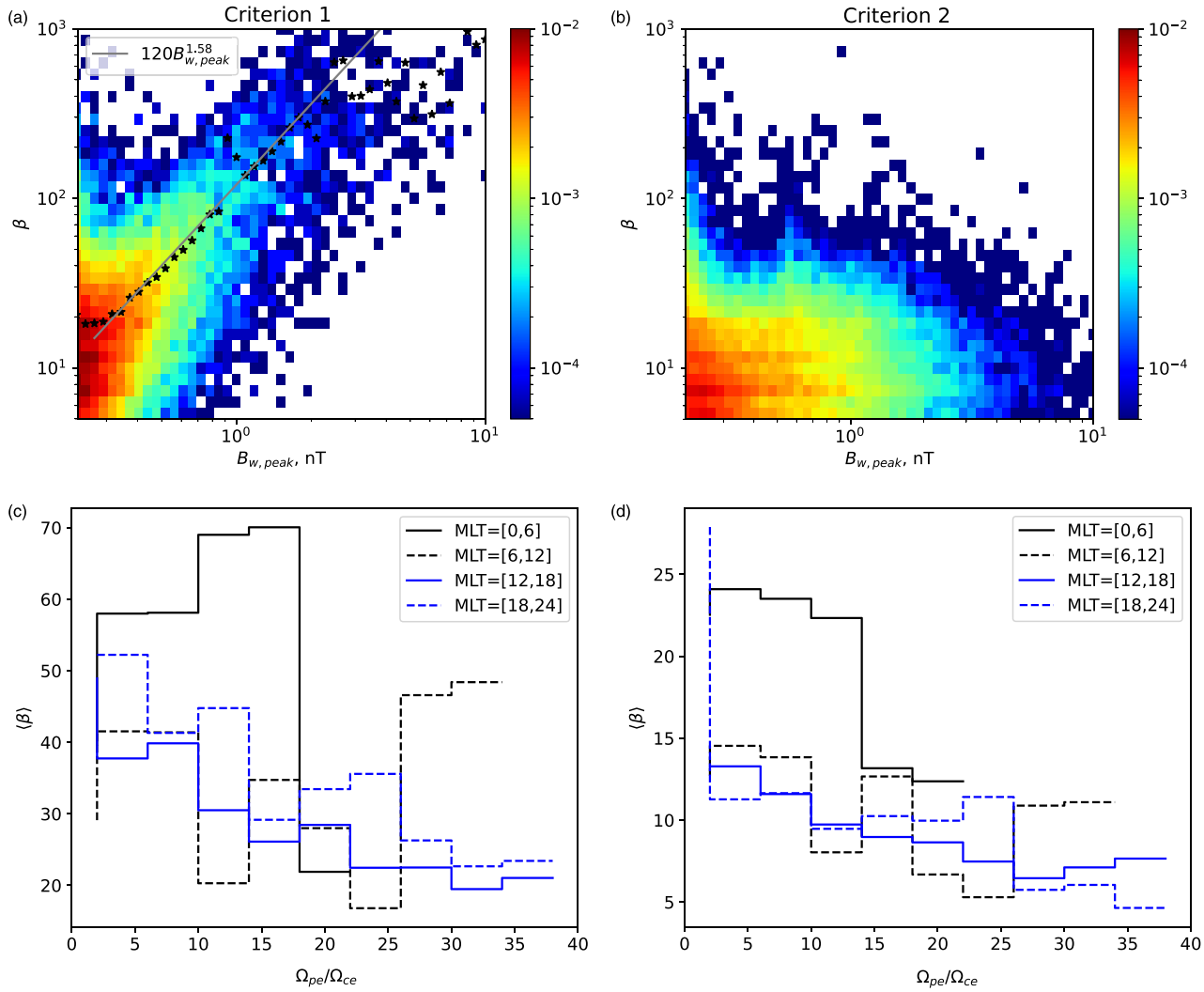

Figure 2. Probability distribution of H-band electromagnetic ion cyclotron wave packets in (β, B_w) space: (a) results from Criterion 1. Crosses denote the mean β for each $B_{w,\mathrm{peak}}$ bin and the solid black line shows the least-square fit $\beta = 120\ B_{w,\mathrm{peak}}^{1.58}$. (b) Results from Criterion 2. (c) Average β as a function of Ω_{pe}/Ω_{ce} and β in 4 different magnetlic local time ranges using Criterion 1. (d) Same as (c) using Criterion 2.

3. Wave-Packet Statistics

Figures 2a and 2b show the probability distribution of wave-packet size β measured using Criteria 1 and 2 (top-left and top-right, respectively), as a function of peak wave-packet amplitude $B_{w,\mathrm{peak}}$, based on 2012–2015 Van Allen Probes data. Most wave-packets have packet sizes in the range of $\beta \sim 5$–30. The results using Criterion 1 demonstrate that wave packet size β increases with peak amplitude approximately as $\beta \approx 120\left(B_{w,\mathrm{peak}}[\mathrm{nT}]\right)^{1.58}$. This trend is roughly consistent with an average wave packet shape $B_w(t)/B_{w,\mathrm{peak}} \approx \epsilon/(|t-t_{\mathrm{peak}}|^{1/1.58}+\epsilon)$ down to the threshold at $B_w = 0.1$ nT, with $\epsilon \ll \max(|t-t_{\mathrm{peak}}|^{1/1.58})$, $B_w(t_{\mathrm{peak}}) = B_{w,\mathrm{peak}}$, and wave-packet size β determined by the temporal scale $\beta \sim |t-t_{\mathrm{peak}}|$. It corresponds to average (and minimum) amplitudes more slowly decreasing far away from $B_{w,\mathrm{peak}}$. Figure 1c shows several examples of packets with this shape. Such a shape is also in agreement with the much shorter size of these packets at half of their peak amplitude using Criterion 2 in Figure 1d. A similar distribution of wave packet sizes and amplitudes has been observed for whistler-mode chorus wave packets (Mourenas et al., 2022; Nunn et al., 2021; Zhang, Demekhov, et al., 2021; Zhang, Mourenas, et al., 2020). Using Criterion 2, the distribution of packet sizes β is less dependent on wave amplitude (compare top-left and top-right panels in Figure 2), which could stem from a different physical origin of the most significant amplitude modulation close to the peak (i.e., likely a nonlinear modulation, perhaps with some wave superposition) compared to other amplitude modulations occurring farther away from the peak.

We also collected the wave frequency, background magnetic field, and the ratio of $\Omega_{pe} = 2\pi f_{pe}$ (electron plasma frequency) to $\Omega_{ce} = 2\pi f_{ce}$ (electron cyclotron frequency) measured simultaneously with each wave-packet. Figures 2c and 2d shows the averaged β of H-band EMIC wave packets as a function of Ω_{pe}/Ω_{ce} in 4 different magnetlic local time (MLT) ranges. Based on both Criteria 1 and 2, the size β of wave-packets at 12–24 MLT decreases by a factor $\approx$2 as Ω_{pe}/Ω_{ce} increases from 5 to 35. There is no clear dependence of β on MLT over 6–24 MLT, whereas β is somewhat larger at 0–6 MLT.

To further understand the properties of EMIC waves and the regime of resonant interactions with electrons, we calculated the resonant interaction's magnetic latitude along the field line for EMIC waves and the inhomogeneity parameter S which controls the dynamics of resonant electrons (Omura & Zhao, 2012). These are explained below.

The wave dispersion relation for proton band EMIC waves can be written as:

$$\left(\frac{kc}{\omega}\right)^2 = 1 - \frac{\Omega_{pe}^2}{\omega(\omega + \Omega_{ce})} - \frac{\Omega_{pi}^2}{\omega(\omega - \Omega_{ci})} \tag{1}$$

where ω is the wave frequency, k is the wave vector, c is the speed of light, Ω_{ps} and Ω_{cs} are plasma frequency and cyclotron frequency for species s (i for proton, e for electron), respectively.

We use a dipole model for the background magnetic field: $B(\lambda) = B_{eq}\sqrt{1 + 3\sin^2\lambda}/\cos^6\lambda = B_{eq} f(\lambda)$ with B_{eq} the magnetic field strength at the equatorial plane and λ the magnetic latitude. Therefore, the electron cyclotron frequency varies with latitude as $\Omega_{ce} = f(\lambda)\Omega_{ce,eq}$. We assume that the plasma frequency $\Omega_{pe} = \sqrt{ne^2/m_e\epsilon_0}$ is a constant along the field line. The resonance condition for relativistic electrons depends on the magnetic latitude:

$$\omega - k(\lambda)v_{\parallel}(\lambda) = -\frac{\Omega_{ce}}{\gamma} \tag{2}$$

where $v_{\parallel}$ is the electron velocity parallel to the background magnetic field and γ is the relativistic factor. At the latitude of cyclotron resonance, the parallel velocity of the resonant electron is determined by γ and the equatorial pitch angle α_{eq}:

$$v_{\parallel}(\lambda) = c\sqrt{1 - \gamma^{-2}}\sqrt{1 - f(\lambda)\sin^2\alpha_{eq}} \tag{3}$$

Combining Equations 1–3 we can get the resonance latitude, λ_R. With ω, $\Omega_{ce,eq}$, and $\Omega_{pe,eq}/\Omega_{ce,eq}$ obtained from observation, we can determine the resonance latitude $\lambda(E, \alpha_{eq})$ at different energies ($E = m_e c^2(\gamma - 1)$) and α_{eq}. Then we calculate the inhomogeneity ratio parameter S, defined as (Omura & Zhao, 2012):

$$S = -\frac{B/B_w}{kv_{\perp}\Omega_{ce}/\gamma}\left(\frac{\omega}{\Omega_e}\left(\frac{v_{\perp}^2 - V_R^2}{2V_p^2} + \frac{V_R^2}{V_g V_p}\right) + \frac{V_R}{\gamma V_p}\right)V_p\frac{\partial\Omega_{ce}}{\partial r_{\parallel}} \tag{4}$$

where $V_R = (\omega + \Omega_{ce}/\gamma)/k$, V_p is the wave phase velocity, V_g is wave group velocity, and

$$\frac{\partial\Omega_{ce}}{\partial r_{\parallel}} = \frac{\partial f(\lambda)}{\partial\lambda}\frac{\partial\lambda}{\partial r_{\parallel}}\Omega_{ce,eq}$$

with $r_{\parallel}$ the direction along the field line. S is a function of resonance latitude. It is proportional to the background field gradient and inversely proportional to the wave intensity. When $|S| < 1$, the waves are intense enough to locally overcome the mirror force and alter the electron trajectory significantly, enabling nonlinear interactions.

Figures 3a and 3d shows the average value of the fraction of H-band EMIC wave packets reaching the threshold $|S| < 1$ for nonlinear wave-particle interaction, as a function of electron equatorial pitch-angle α_{eq} and energy E, for Criterion 1 and 2, respectively. Note that this fraction is weighted by packet duration, that is, it is the ratio of the duration of wave packets with $|S| < 1$ to the total time of wave-packet measurements. Figures 3b and 3c shows the average amplitude of waves with $|S| < 1$ in the same format, with the contours transferred from Figures 3a and 3d. Figures 3c and 3f shows the wave-packet length β, in the same format as Figures 3b and 3c. Based on Criterion 1, most packets allowing nonlinear interaction are relatively long, with an average size β = 30–500. The fraction of wave packets reaching the threshold for nonlinear interaction varies between 3% and 10% and

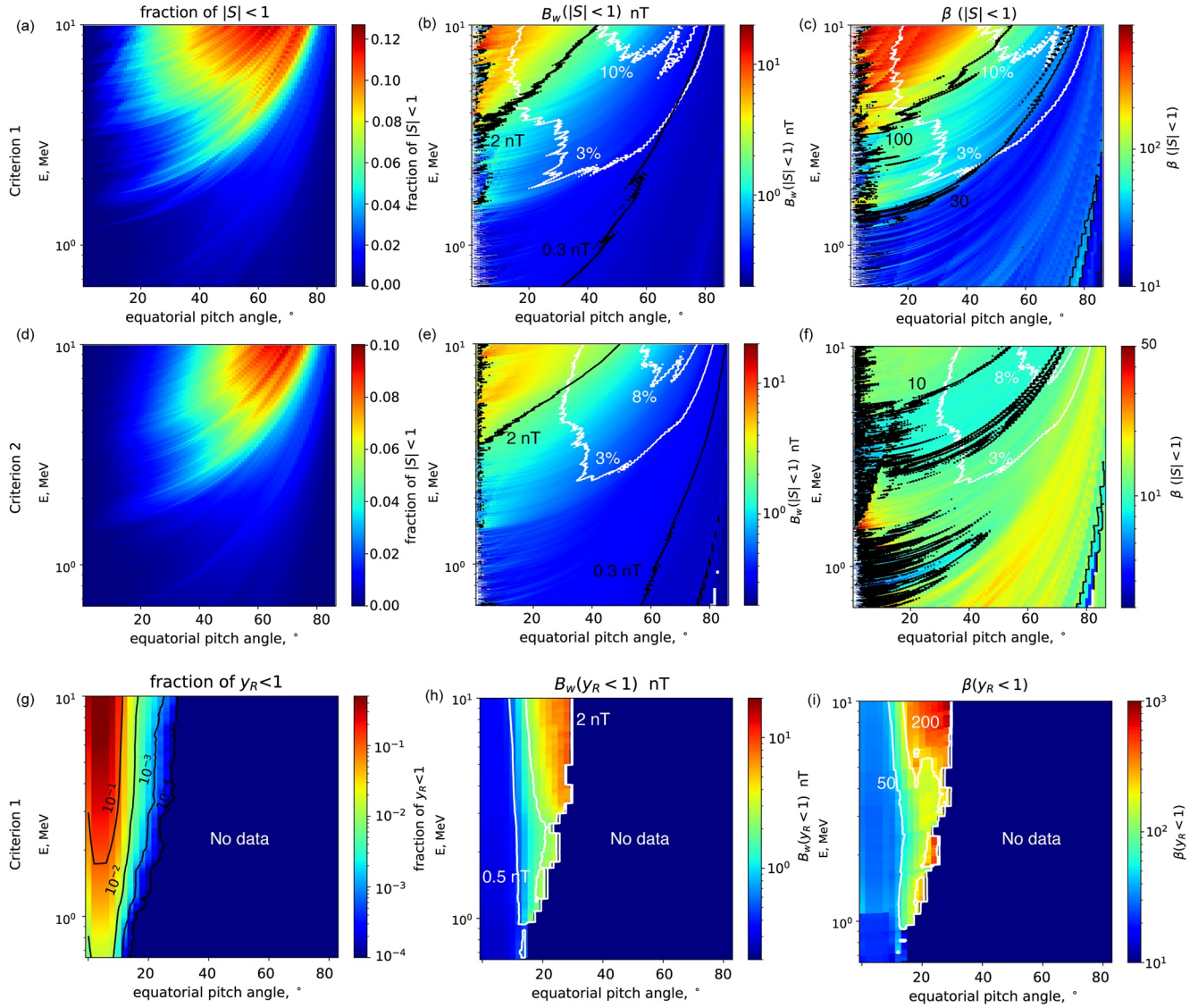

Figure 3. (a) Fraction of H-band electromagnetic ion cyclotron (EMIC) wave-packets with $|S| < 1$ as a function of electron energy E and equatorial pitch-angle α_{eq}, using Criterion 1. (b) Average peak wave amplitude $B_{w,\mathrm{peak}}$ of $|S| < 1$ wave-packets based on Criterion 1. (c) Average size $\langle\beta\rangle$ of $|S| < 1$ wave-packets using Criterion 1. Contours in (b,c) show levels of the distribution from (a). (d,e,f) Same as (a,b,c) based on Criterion 2. (g) Fraction of H-band EMIC wave-packets (based on Criterion 1) with $y_R < 1$ as a function of electron energy E and equatorial pitch-angle α_{eq}. (h) Average peak wave amplitude $B_{w,\mathrm{peak}}$ of $y_R < 1$ wave-packets based on Criterion 1. (i) Average size $\langle\beta\rangle$ of $y_R < 1$ wave-packets using Criterion 1.

corresponds to peak amplitudes $B_{w,\mathrm{peak}} \sim 0.3$–$2$ nT. Noticeably, a significant fraction (>10%) of EMIC wave packets, mostly with amplitudes larger than 1 nT, are able to interact nonlinearly with >2 MeV electrons around $\alpha_{\mathrm{eq}} \sim 40°$–$60°$. However, using Criterion 2, we show that most of these packets with $|S| < 1$ contain a strong inner modulation of B_w by at least a factor of 2 around each peak, $B_{w,\mathrm{peak}}$, corresponding to a shorter average packet size $\beta \sim 10$–15. Such a strong wave amplitude modulation may reduce the effectiveness (duration) of nonlinear electron trapping, especially in the presence of simultaneous frequency and phase jumps in-between packets (Grach et al., 2021; Liu et al., 2018; Nakamura et al., 2015; Usanova et al., 2010), as in the case of realistic short chorus wave packets (Z. An, Artemyev, et al., 2022; Tao et al., 2013; Zhang, Agapitov, et al., 2020).

The inhomogeneity ratio given by Equation 4 describes wave-particle resonant interactions for not-too-small electron pitch-angles or sufficiently large electron magnetic moments. When the electron pitch-angle is small enough, another nonlinear regime, the so called *force bunching*, becomes important, and could potentially prevent electron precipitation by advecting such electrons toward larger pitch-angles (see discussion in Albert

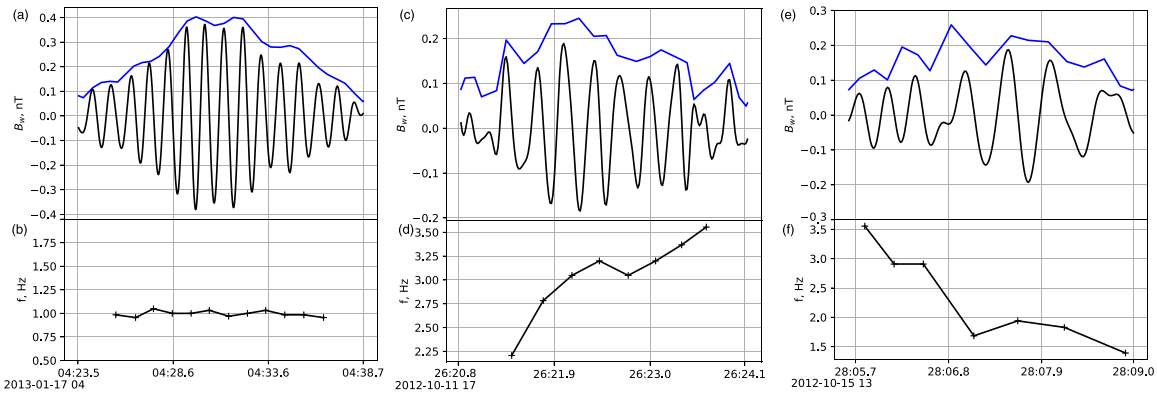

Figure 4. Three examples of wave packets with $f \approx$ const (a), $\partial f/\partial t > 0$ (b), and $\partial f/\partial t < 0$ (c).

et al., 2022; Bortnik et al., 2022; Grach & Demekhov, 2020, and references therein). Force bunching plays an important role in the formation of precipitation fluxes (see Grach et al., 2021, 2022; Hanzelka, Li, & Ma, 2023), and can be effective for short packets, when trapping doesn't occur even for $|S| < 1$ because of the short packet length (Grach et al., 2021, 2022). This effect can be characterized by the parameter y_R (or $\delta = y_R - 1$), an analog of S, but derived for a system with small pitch-angles: the force bunching regime corresponds to $y_R < 1$ (see Albert et al., 2021; Artemyev et al., 2021). Figure 3 (g) shows the fraction of H-band EMIC wave packets reaching the threshold $y_R < 1$, and panels (h) and (i) show the average peak wave amplitude and packet size of waves satisfying $y_R < 1$. For electrons with pitch-angles below 10°, force bunching occurs for almost ∼10% of the observed waves, with an average wave-packet peak amplitude of ∼0.5 nT. Most of such intense wave packets are not too short, $\beta \sim 50$, and, thus, force bunching will compete with phase trapping and scattering for determining the magnitude of electron precipitation (see discussion in Bortnik et al., 2022; Grach et al., 2022; Hanzelka, Li, & Ma, 2023).

4. Wave Frequency Variations

A coherent wave frequency variation within a wave-packet train is a natural element of EMIC waves (often forming rising tones—e.g., see Shoji & Omura, 2013), and it can alter nonlinear resonant interactions (e.g., Grach et al., 2021; Kubota & Omura, 2017; Omura & Zhao, 2013). However, wave frequency can also significantly vary inside wave packets and, because such variations are not always coherent, they may terminate nonlinear resonant wave-particle interaction, thereby significantly reducing the efficiency of nonlinear phase trapping (see discussion in Z. An, Artemyev, et al., 2022; Zhang, Agapitov, et al., 2020; Zhang, Mourenas, et al., 2020). Figure 4 shows three examples of wave-packets with nearly constant frequency, rising frequency ($\partial f/\partial t > 0$) and falling frequency ($\partial f/\partial t < 0$). The frequency change is determined by linear regression of the half-wave periods obtained from two successive zero points of the transverse component of the wavefield. We calculated $\partial f/\partial t$ inside each wave-packet. The wave-packet distribution in (β, $\partial f/\partial t$) space for the two Criteria of wave-packet selection are shown in Figure 5. Because there are often frequency jumps near the edges of packets, we calculated the linear regression only for the center part of each wave-packet, that is, where B_w is above the 25th percentile of the amplitudes inside the packet.

As seen in Figures 5a and 5b, obtained using Criteria 1 and 2, respectively, most of the H-band EMIC wave packets have a frequency sweep rate $\partial f/\partial t \approx 10^{-3} - 10^{-1}$ Hz/s, with no clear dependence on the peak packet amplitude $B_{w,\mathrm{peak}}$. This is similar to the range of EMIC frequency sweep rates obtained in previous case studies (Nakamura et al., 2015, 2019). The range of measured sweep rates in our statistics agrees with typical sweep rates derived from the nonlinear theory of EMIC wave growth for realistic wave amplitude and plasma parameters (Omura et al., 2010). Note, however, that the frequency within a given observed packet can often show significant oscillations, even within relatively short packets (e.g., see Figures 4d and 4f).

Figures 5c and 5d show that most EMIC wave packets are clustered between two thin solid black lines, regardless of the criterion (1 or 2) used to determine packet size. The lowest thin solid black line in Figures 5c–5f shows a normalized frequency sweep rate $(\partial f/\partial t)/f^2 = 10^{-4}$, independent of β. It shows low or moderate frequency sweep rates, which increase linearly with $B_{w,\mathrm{peak}}$ in Figures 5a and 5b, as expected from the nonlinear theory of EMIC

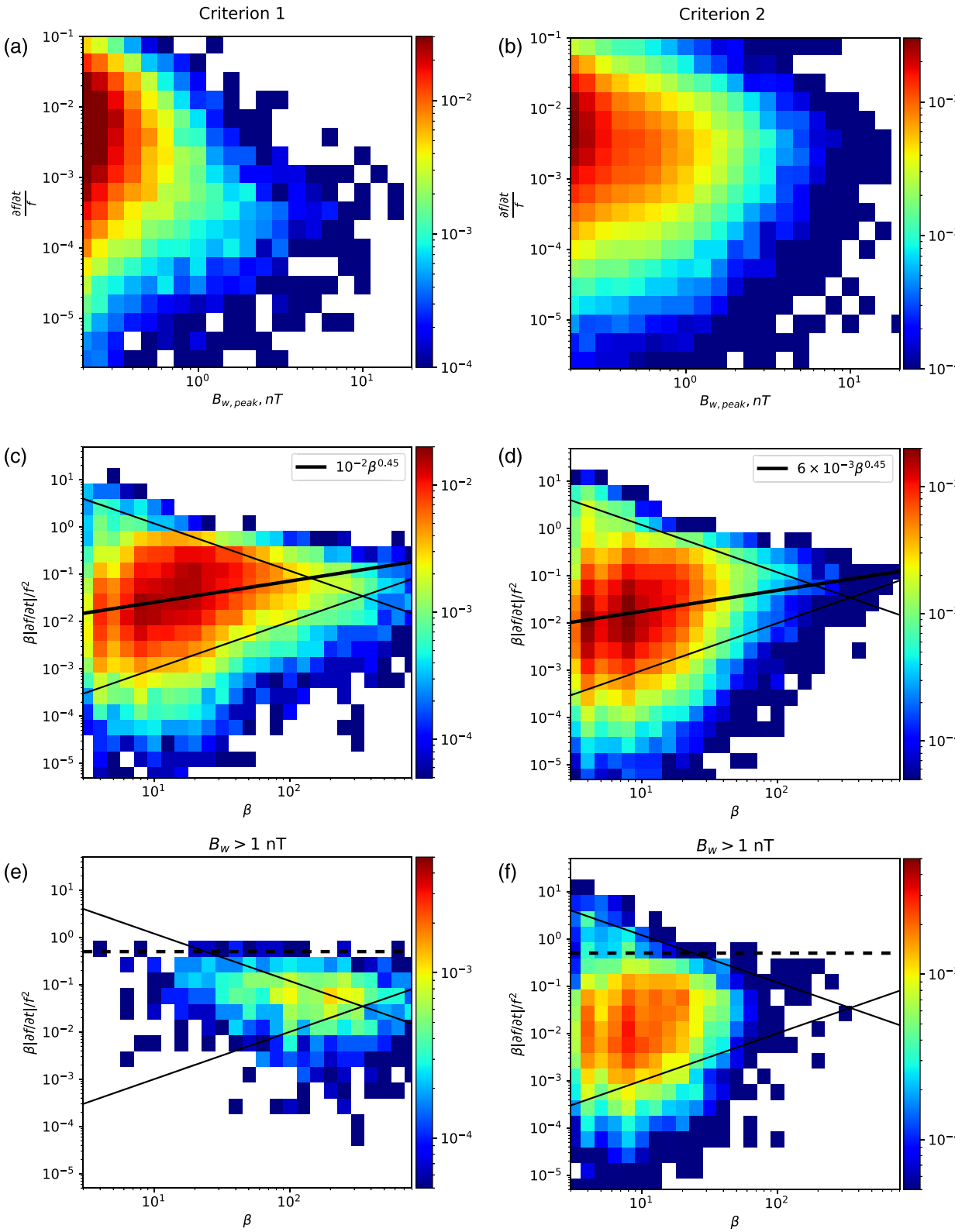

Figure 5. Distribution of observed H-band electromagnetic ion cyclotron (EMIC) wave packets in ($B_{w,\mathrm{peak}}$, $\partial f/\partial t/f$) space for criteria 1 (a) and 2 (b), where $\partial f/\partial t$ is determined by linear fitting of the middle portion of each wave-packet. (c,d) Same as (a,b) for the distribution of packets in $\left[\beta, \beta(\partial f/\partial t/f)/f^2\right]$ space. The lowest and highest thin solid black lines show two theoretical scalings based on the nonlinear theory of EMIC wave growth and wave superposition, respectively (see text). The thick solid black line shows the least squares power-law fit to the full distribution. (e, f) Same as (c, d) for intense packets with $B_{w,\mathrm{peak}} > 1$ nT. A dashed black line shows the scaling corresponding to the maximum frequency sweep rates due to the limited frequency range of EMIC waves.

wave growth (Omura et al., 2010; Shoji et al., 2018). The highest thin black line in Figures 5c–5f shows a normalized frequency sweep rate $(\partial f/\partial t)/f^2 = 12/\beta^2$ decreasing as the packet size β increases. It represents the typical scaling of the average frequency sweep rate with β, produced by the superposition of two waves of slowly varying amplitude and frequency, as in the case of whistler-mode chorus wave packets (see model details in Zhang, Mourenas, et al., 2020). Based on the observed trends in the distribution of sweep rates displayed in Figures 5c and 5d, short packets with $\beta < 50$ and high frequency sweep rate, such that $3/\beta^2 < (\partial f/\partial t)/f^2 < 30/\beta^2$, are probably mainly formed by such wave superposition around their peak power (where $B_w(t) > B_{w,\mathrm{peak}}/2$). In contrast, longer packets with $\beta > 50$ and/or packets with a lower sweep rate $(\partial f/\partial t)/f^2 < 1/\beta^2$ are probably mainly formed by nonlinear trapping-induced amplitude modulation during wave growth (Mourenas et al., 2022; Nakamura et al., 2015; Shoji & Omura, 2013; Tao et al., 2017), without significant superposition. The distribution of packet occurrences in Figures 5c and 5d exhibits an intermediate trend due to the interplay of different sweep rates. Low to moderate nonlinear sweep rates remain relatively independent of packet size. In contrast, high sweep rates, which arise from wave superposition, decrease as the packet size increases. This combination of effects results in the intermediate trend observed between the two thin black curves in the figures. The least squares power-law fit of this global trend is $(\partial f/\partial t)/f^2 \approx 10^{-2} \times \beta^{-0.55}$ (shown by a thick black line). This global trend is close to the expected trend due to nonlinear trapping-induced modulation (with $(\partial f/\partial t)/f^2 \propto$ const) than to the trend corresponding to wave superposition (with $(\partial f/\partial t)/f^2 \propto \beta^{-2}$). This suggests a dominant role of trapping-induced amplitude modulation in the formation of EMIC wave packets, contrary to the case of short chorus wave packets (Zhang, Mourenas, et al., 2020).

The decreasing trend toward larger β in the distribution of the highest sweep rates of the most intense packets (with $B_{w,\mathrm{peak}} > 1$ nT) in Figure 5f, determined using Criterion 2, probably means that such packets (or sub-packets) are mainly formed by wave superposition near their peak power. However, the increasing trend of the distribution of packets with low to moderate $\beta(\partial f/\partial t)/f^2$ as β increases in Figure 5f, suggests that the majority of these packets are formed by nonlinear modulation. Using Criterion 1 in Figure 5e to examine the same packets with $B_{w,\mathrm{peak}} > 1$ nT over their whole length down to 0.2 nT, shows that they are very long ($\beta = 50$–1,000), and that their normalized sweep rate over this full length becomes nearly independent of β, with a maximum scaling $\beta(\partial f/\partial t)/f^2 \approx 0.5$ independent of β (see dashed black line). The maximum sweep rate of long and intense lower-band chorus wave packets has a similar scaling, $(\partial f/\partial t)/f^2 \sim 1/\beta$, which stems from the limited frequency bandwidth of lower-band chorus waves (Teng et al., 2017; Zhang, Mourenas, et al., 2020). Similarly, the maximum normalized frequency bandwidth of intense H-band EMIC waves is typically limited to $\Delta f/f_{cp} \sim 0.2$ (with an average frequency $\langle f\rangle/f_{cp} \sim 0.4$ at peak power), probably due to both strong damping as f increases toward the proton gyrofrequency f_{cp} and a narrow stop band above the helium gyrofrequency at $f_{cp}/4$ in a realistic plasma composed of protons with a small fraction of helium ions (Kersten et al., 2014; Ross et al., 2021). Since the duration of these packets is $\Delta t = \beta/\langle f\rangle$, this gives an upper limit $\max(\beta\,(\partial f/\partial t)/f^2) = \beta\,(\Delta f/\Delta t)/\langle f\rangle^2 \sim 0.2\,f_{cp}/\langle f\rangle \sim 0.5$ for the longest packets with $\beta > 50$ and high sweep rates. The scaling of this theoretical upper limit (shown by a dashed black line) agrees well with the maximum observed values of $\beta\,(\partial f/\partial t)/f^2$ for long ($\beta > 50$) and intense ($B_{w,\mathrm{peak}} > 1$ nT) EMIC wave packets in Figures 5e and 5f.

Significant, random frequency jumps are observed near the edge of EMIC wave packets. Figures 6a–6c provide examples of fast frequency increases or decreases (with only weak simultaneous wave-normal angle Φ variations) at the boundary of several packets, where the wave amplitude is small. We use $f/\langle f\rangle_{B_w} - 1$ to describe the distribution of frequency variations inside each wave packet where $\langle f\rangle_{B_w}$ is the average frequency weighted by wave amplitude. Figure 6d shows that the distribution of relative frequency variations $f/\langle f\rangle_{B_w} - 1$ is quite wide, with ~10% of the wave frequencies reaching $f \sim 0.6\langle f\rangle_{B_w}$ and ~0.2% reaching $f \sim 2\langle f\rangle_{B_w}$. Similar results have been obtained for the distribution of frequency variations inside chorus wave packets (Zhang, Mourenas, et al., 2020), suggesting the presence of similar physical phenomena in both EMIC and chorus wave packets, such as wave superposition and nonlinear amplitude modulation.

5. Implications for Electron Precipitation by Intense H-Band EMIC Wave Packets

In this section, we use our statistics of H-band EMIC wave packets to determine the main (MLT,Ω_{pe}/Ω_{ce}) ranges of high-energy electron precipitation by such intense packets, and the relative importance of quasi-linear, nonlinear, and so-called nonresonant interactions for electron precipitation at high and low energy.

Figure 7 shows that the fraction of H-band EMIC wave packets with $|S| < 1$ for $E = 3$–10 MeV and $\alpha_{eq} = 40°$–60° is larger when $\Omega_{pe}/\Omega_{ce} > 10$ than when $\Omega_{pe}/\Omega_{ce} < 10$ (~50–80% vs. ~20–50%), but also sensibly larger at 4–11

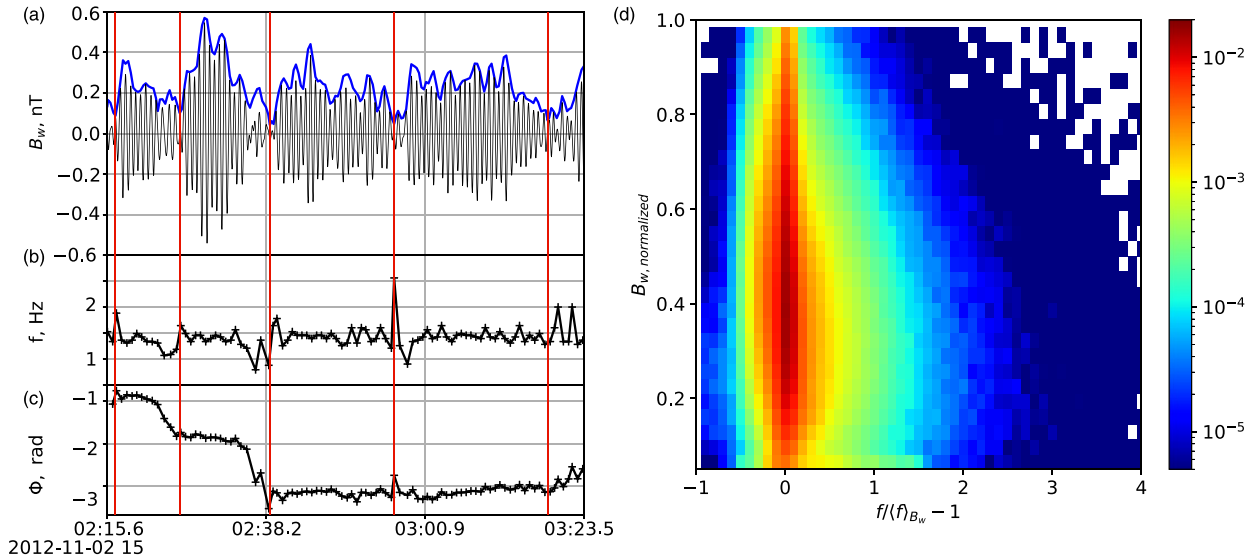

Figure 6. (a,b,c) Amplitude, frequency, and wave-normal angle variations of examples of H-band electromagnetic ion cyclotron (EMIC) wave packets. (d) Distribution of H-band EMIC wave packets in $\left(f/\langle f\rangle_{B_w} - 1,\ B_w/B_{w,\max}\right)$ space for all wave packets in out database. $B_{w,\max}$ is the maximum amplitude for each wave-packet.

MLT (~70–80%) than at 12–24 MLT (~50–60%). This implies that nonlinear interactions should be on average more important at 4–11 MLT than at 12–24 MLT for electrons within these energy and pitch-angle ranges, which are the most likely to experience nonlinear trapping for typical wave and plasma parameters (Grach et al., 2022; Kubota & Omura, 2017; Omura & Zhao, 2012). However, Figures 7b and 7d suggest that nonlinear interactions probably play a significant role in the precipitation of >3 MeV electrons by H-band EMIC waves when $\Omega_{pe}/\Omega_{ce} > 10$ over the whole 5–24 MLT domain, through an initial nonlinear trapping at $\alpha_{eq} = 40°$–$60°$ by the highest amplitude part of an intense wave packet, leading to a rapid decrease of α_{eq}, followed by scattering into the loss cone by the lower amplitude part of this packet or other low amplitude packets (Grach et al., 2022; Kubota & Omura, 2017; Nakamura et al., 2019; Omura & Zhao, 2012). Figures 7a and 7c also show that the absolute number of wave packets with $|S| < 1$ is larger at 9–20 MLT and when $\Omega_{pe}/\Omega_{ce} < 25$. This is consistent with the lower occurrence rate of all H-band EMIC waves and their reduced average intensity at 0–8 MLT compared with 8–20 MLT and for $\Omega_{pe}/\Omega_{ce} > 25$ compared with $\Omega_{pe}/\Omega_{ce} < 25$ (Ross et al., 2021).

Figure 8a shows the statistical distribution of the average of the normalized wave power $\langle B_w^2(\omega/\Omega_{ci})/B_{w,\text{peak}}^2\rangle$ inside H-band EMIC wave packets (determined using Criterion 1) in the 10–16 MLT sector where low energy electron precipitation is most effective (Angelopoulos et al., 2023), for three Ω_{pe}/Ω_{ce} ranges (0–5, 5–15, >15). We only kept wave packets determined based on Criterion 1, with a peak amplitude $B_{w,\text{peak}} > 0.2$ nT occurring at $\omega/\Omega_{ci} \in [0.4, 0.5]$ where the most intense H-band waves are statistically observed (Zhang et al., 2016). In addition, we only keep waves above 3 times the wave power noise level in this frequency range, estimated based on measurements performed at 0–6 MLT during very quiet periods without EMIC waves. This way, wave half-periods at the edge of wave packets are automatically excluded when their amplitude is less than 3 times the noise level, to prevent a potential underestimation or overestimation of the wave period caused by this noise. For each packet, we calculated $B_w(\omega/\Omega_{ci})$ within the packet (during each half wave period), as well as the maximum frequency $\omega_{\max}$ reached within this packet, and a null amplitude, $B_w(\omega/\Omega_{ci}) = 0$, was assigned to frequencies $\omega > \omega_{\max}$ not present within the packet. Finally, an averaging was performed over all these packets.

Figures 8a–8c show: the average wave power spectrum of typical intense packets; of the most intense packets with $B_{w,\text{peak}} > 1$ nT; and of the shortest packets with $\beta < 10$. The wave power within these packets remains surprisingly elevated up to high frequencies, reaching on average ~1.5–3% of their peak power $B_{w,\text{peak}}^2$ at $\omega/\Omega_{ci} = 0.7$ –0.9, with a slightly higher level in the most intense packets and a lower level (~0.5–1%) in the shortest packets. Taking into account the smaller data set available at 0–6 MLT, there is no significant dependence on the electron plasma frequency to gyrofrequency ratio Ω_{pe}/Ω_{ce}. Since sub-relativistic (<0.5 MeV) electron precipitation through cyclotron resonance with H-band EMIC waves requires a high ratio $\Omega_{pe}/\Omega_{ce} > 10$–15 and a high frequency $\omega/\Omega_{ci} > 0.7$ (Summers & Thorne, 2003), these results imply that cyclotron resonance with intense H-band EMIC

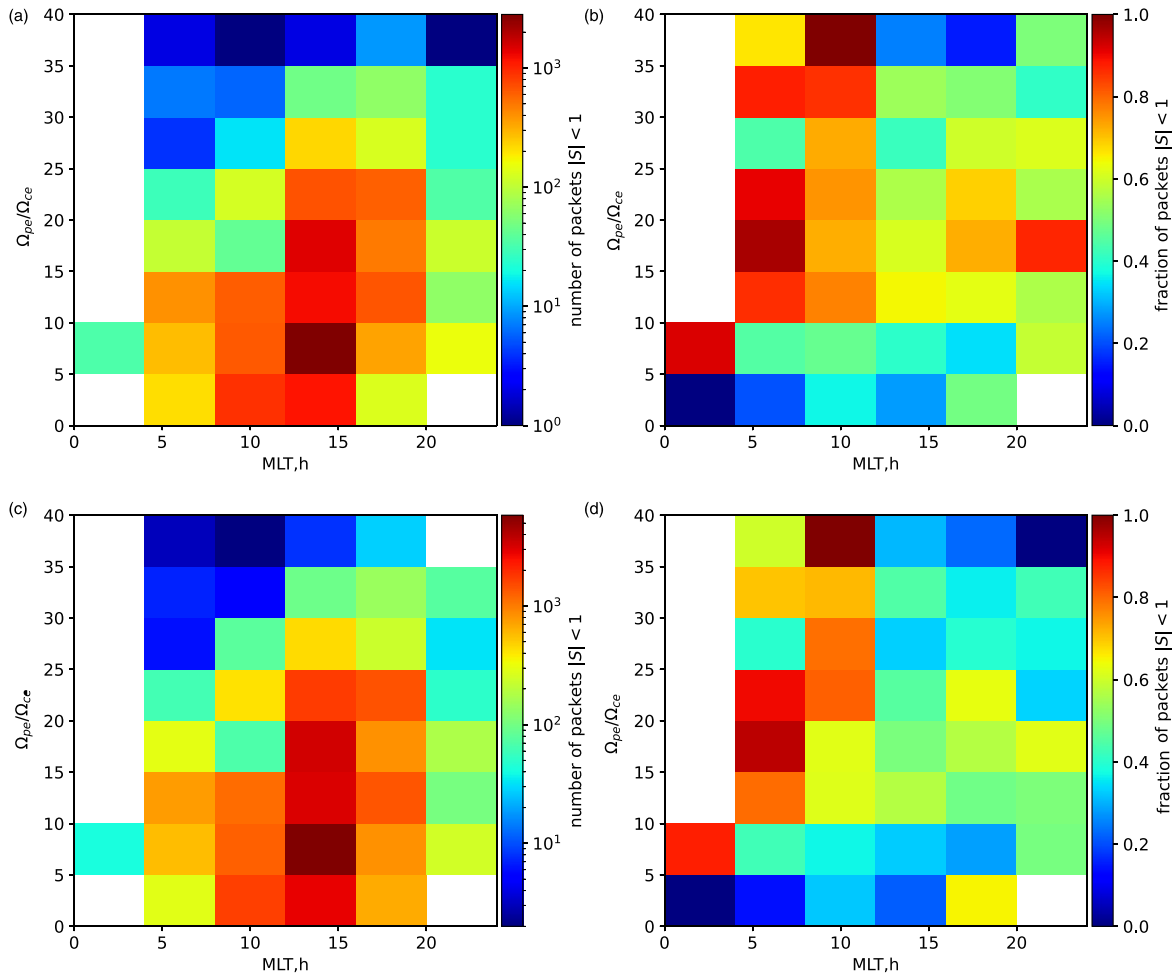

Figure 7. Number of H-band electromagnetic ion cyclotron (EMIC) wave packets (a,c) and fraction of H-band EMIC wave packets (b,d) with $|S| < 1$ for $E = 3 - 10$ MeV and $\alpha_{eq} = 40°–60°$ in (magnetlic local time, Ω_{pe}/Ω_{ce}) space, for criteria 1 (a,b) and 2 (c,d). Note that the gap in MLT = 0–4 is due to the absence of events.

wave packets in high-density regions likely plays an important role in the sub-relativistic electron precipitation frequently observed during conjunctions with EMIC wave bursts measured near the equator (Angelopoulos et al., 2023; Capannolo, Li, Ma, Shen, et al., 2019; Hendry et al., 2017, 2019; Zhang, Mourenas, et al., 2021), especially when they are not too short ($\beta > 10$) and reach high peak amplitudes $B_{w,\mathrm{peak}} > 1$ nT.

Indeed, Figures 8b and 8c indicate that the most intense and longest packets are comparatively more likely to produce sub-relativistic electron precipitation through cyclotron resonance. Although this may suggest that nonlinear interactions (trapping) with intense packets could be important for sub-relativistic electron precipitation, it is worth noting that only a small fraction, ~3–8%, of the packets can reach the threshold $|S| < 1$ for nonlinear interaction with 0.3–0.8 MeV electrons in Figure 3, only at $\alpha_0 > 40°$. Moreover, Figure 8f shows that inside all packets at 10–16 MLT, the average power $\langle B_w^2 \rangle$ of waves present at $\omega/\Omega_{ci} \sim 0.7$ when $\Omega_{pe}/\Omega_{ce} > 15$ corresponds to low amplitudes $B_w \sim 0.1$ nT that may be insufficient for trapping. Therefore, the most probable origin of sub-relativistic electron precipitation is electron scattering near the loss cone (Kubota & Omura, 2017) through cyclotron resonance with the higher-frequency, lower-power part of intense H-band EMIC wave packets. A similar conclusion has recently been drawn from the good agreement, over a wide energy range (0.2–1.5 MeV), between average precipitating to trapped electron flux ratios measured by the low-altitude Electron Losses and Fields Investigation (ELFIN) CubeSats at $L \sim 5–6$ in the noon-dusk sector and flux ratios inferred from electron quasi-linear diffusion through cyclotron resonance with statistical H-band EMIC wave power spectra measured by the Van Allen Probes (Angelopoulos et al., 2023), although that study could not identify the dominant role of intense packets.

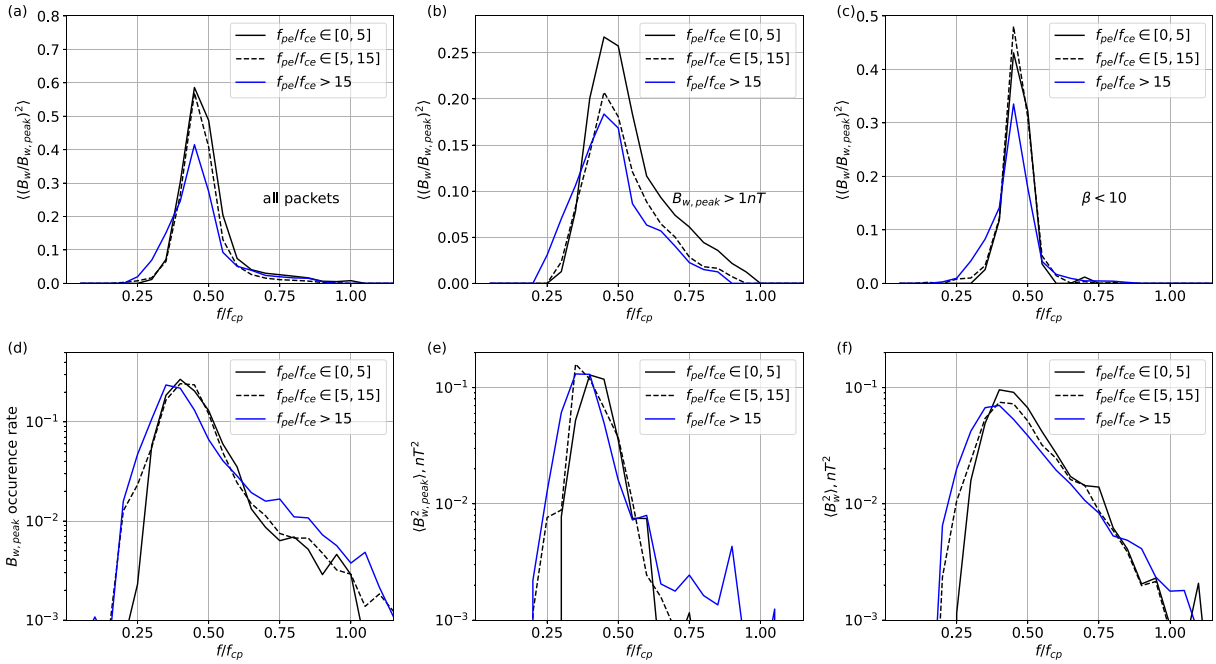

Figure 8. (a) Statistical distribution of $\langle B^2_w(\omega/\Omega_{ci})/B^2_{w,\text{peak}} \rangle$ as a function of ω/Ω_{ci} inside H-band electromagnetic ion cyclotron wave packets (determined using Criterion 1) in the 10–16 magnetic local time (MLT) sector, such that their peak amplitude $B_{w,\text{peak}}$ is reached at $\omega/\Omega_{ci} \in [0.40, 0.50]$, for three Ω_{pe}/Ω_{ce} ranges (0–5, 5–15, >15). (b,c) Same as (a) for all packets determined using Criterion 1 in the 10–16 MLT sector with $B_{w,\text{peak}} > 1$ nT; and for the fraction of packets with $\beta < 10$, respectively. (d,e,f) The occurrence rate of the peak amplitude of a packet as a function of ω/Ω_{ci}; $\langle B^2_{w,\text{peak}}(\omega/\Omega_{ci}) \rangle$; and $\langle B^2_w(\omega/\Omega_{ci}) \rangle$, respectively, for all packets determined using Criterion 1 in the 10–16 MLT sector, for the same Ω_{pe}/Ω_{ce} ranges.

Interestingly, the shortest packets, with $\beta < 10$, still comprise a non-negligible wave power at high frequencies $\omega/\Omega_{ci} \approx 0.7$, which may be surprising at first sight since all packets selected in Figures 8a–8c) reach their maximum power at $\omega/\Omega_{ci} = 0.4$–0.5. But Figure 5 shows that short packets can have high frequency sweep rates $\partial f/\partial t > 0.05$ Hz/s, sufficient to reach such high frequencies over less than 10 wave periods. Figure 6d also shows that frequency oscillations within packets often reach ∼1.6–2 times their average frequency, consistent with results in Figure 8c. Figure 8c indicates that short EMIC wave packets, which may be more capable of producing nonresonant scattering of sub-relativistic electrons (Chen et al., 2016; X. An, Artemyev, et al., 2022), similarly contain a significant fraction of average wave power at high frequencies $\omega/\Omega_{ci} \sim 0.7$, much higher than the frequency $\omega/\Omega_{ci} \sim 0.4$–$0.5$ of the main waves at peak power. This indeed allows sub-relativistic electron scattering via cyclotron resonance with the high-frequency, high-k tail of the EMIC wave power spectrum, as discussed earlier. Accordingly, EMIC wave-packet statistics presented in Figure 8 suggest that resonant scattering by the upper-frequency tail of the wave power spectrum of intense packets may be sufficiently frequent to account for most events of sub-relativistic electron precipitation.

It is worth emphasizing again here that high $\omega/\Omega_{ci} > 0.7$ H-band EMIC waves naturally correspond, through their dispersion relation, to high wave numbers k (Denton et al., 2019; Summers & Thorne, 2003), allowing cyclotron resonance with electrons of lower energy than in the case of more typical lower-frequency waves (e.g., see Section 1.3). Basically, a high frequency corresponds to a short time interval $\sim\pi/\omega$ between two successive changes of sign of the wave electric field, which should translate in space into a short distance $\sim\pi/k$ between similar changes of sign, with $k = \omega \times 1/v_{ph}$ and v_{ph} the wave phase velocity for EMIC waves obeying the dispersion relation. Even for high ω/Ω_{ci} waves produced by wave superposition, one still expects to get $k \sim \omega \times (1/v_{ph}$ to $1/v_g)$, where the parallel group velocity v_g is lower than v_{ph} for $\omega/\Omega_{ci} > 0.5$, giving k values at least as high as based on the dispersion relation. From another perspective, the k distribution due to the superposition of two or more waves of slowly varying amplitudes is expected to be similar to the distribution of ω/Ω_{ci} values due to superposition, with a similar heavy tail up to at least $\sim 2\langle k \rangle$ (Zhang, Mourenas, et al., 2020). For $\langle \omega/\Omega_{ci} \rangle \sim 0.45$, $k \sim 2\langle k \rangle$ corresponds to $\omega/\Omega_{ci} \sim 0.7$ via the dispersion relation. This suggests that most waves with $\omega/\Omega_{ci} \sim 0.7$–$0.8$ in Figures 8a–8c should indeed reach cyclotron resonance with sub-relativistic electrons.

Figures 8d and 8e show the occurrence rate of the peak amplitude of a packet and the average peak power $\langle B^2_{w,\mathrm{peak}} \rangle$ (weighted by the occurrence rate of peak power in each normalized frequency bin) as a function of ω/Ω_{ci}, for all packets at 10–16 MLT selected using Criterion 1. We only plot waves with a peak amplitude at $\omega/\Omega_{ci} \leq 1.15$ to exclude other types of waves, such as ion Bernstein modes, while retaining waves at $\omega/\Omega_{ci} \simeq 1.0$–$1.1$ that might still be EMIC waves (e.g., see Wang et al., 2023). While most packets (~60%) reach their peak power $B^2_{w,peak} > 0.1\,\mathrm{nT}^2$ at moderate frequencies $\omega/\Omega_{ci} \sim 0.35$–$0.5$, there is also a finite fraction (~5%) of intense packets reaching a peak amplitude $B_{w,\mathrm{peak}} \sim 0.1$ nT at $\omega/\Omega_{ci} \sim 0.75 - 0.90$ when $\Omega_{pe}/\Omega_{ce} > 15$, corresponding to a much lower $\langle B^2_{w,\mathrm{peak}} \rangle \sim 0.0025\ \mathrm{nT}^2$. Finally, Figure 8f shows the average power $\langle B^2_w \rangle$ of H-band EMIC waves from intense packets at 10–16 MLT that are present in each ω/Ω_{ci} bin. Waves at high frequencies $\omega/\Omega_{ci} \sim 0.7$–$0.8$ still reach root-mean-square amplitudes of ~0.1 nT.

The wave power distributions provided in Figures 8a and 8b could be used to calculate the ratio of quasi-linear diffusion rates at low and high energy from the subset of EMIC waves within such intense packets, for comparisons with events of rapid electron loss, where precipitation at low energy 0.2–0.7 MeV is much less efficient than above 2 MeV but still discernible in low-altitude spacecraft observations during conjunctions with EMIC wave bursts measured near the equator (Angelopoulos et al., 2023; Capannolo et al., 2023; Capannolo, Li, Ma, Shen, et al., 2019; Hendry et al., 2017; Zhang, Mourenas, et al., 2021).

6. Discussion and Conclusions

Although the present results are based on statistics of individual EMIC wave-packets, EMIC wave characteristics are expected to remain roughly similar within the entire EMIC wave source region, of typical spatial extent ~0.5 R_E to ~1 R_E at the equator (Blum et al., 2016, 2017). Therefore, EMIC wave-packet characteristics, specific inside each wave source region, are expected to determine the properties of the associated electron precipitation over a relatively large spatial domain, much larger than the domains of precipitation bursts driven by individual whistler-mode wave packets (see discussion in Zhang et al., 2023). Figure 9 shows an example of simultaneous EMIC wave-packet observations by two THEMIS spacecraft (Angelopoulos, 2008) with ~1 R_E azimuthal separation: although wave spectra and individual wave-packets show some differences, the general wave-packet characteristics (number of wave periods, average frequency, and frequency jumps at the wave-packet edges) remain similar. Further investigations of multi-spacecraft missions will be needed to statistically confirm this expected homogeneity of EMIC wave-packet characteristics within a given wave source region. In addition, the spatial scale of the region occupied by EMIC waves increases during their propagation to middle latitudes (Hanzelka, Li, Ma, Qin, et al., 2023; Kim & Johnson, 2016). This should further increase the spatial extent of electron precipitation driven by similar EMIC wave-packets.

In this study, we used 3 years of Van Allen Probe observations to provide the distributions of wave amplitudes, wave-packet sizes, and rates of frequency variations within individual intense H-band EMIC wave-packets. We found that most of such intense wave-packets are short, with ~10 wave periods each, and that up to 10% of such packets can attain amplitudes that enable nonlinear resonant interaction with multi-MeV electrons. Up to 3% of these packets can reach nonlinear resonant interaction with 2 MeV electrons, mainly for equatorial pitch-angles >20°–30°. Frequency variations within packets often reach ~50–100%. We showed that such wave packet characteristics are likely mainly due to the presence of amplitude modulations due to nonlinear trapping during EMIC wave growth (Nakamura et al., 2015; Shoji & Omura, 2013), although a significant fraction of the packets (especially packets with high frequency sweep rates) probably result from wave superposition. In comparison, short chorus wave packets mostly result from wave superposition (Nunn et al., 2021; Zhang, Demekhov, et al., 2021; Zhang, Mourenas, et al., 2020). The range of observed frequency sweep rates within packets agrees well with the nonlinear theory of EMIC wave growth (Omura et al., 2010).

We examined the implication of H-band EMIC wave packet characteristics for electron precipitation and the regime of wave-particle interactions. The occurrence rate of intense wave packets potentially reaching the nonlinear regime (with $|S| < 1$ for E = 3–10 MeV and α_{eq} = 40°–60°) was found to have a broad maximum at 5–24 MLT and at $\Omega_{pe}/\Omega_{ce} > 10$, suggesting an important role of such intense packets in rapidly transporting multi-MeV electrons to lower pitch-angles α_{eq} = 10°–20° through trapping, before a subsequent scattering eventually leads to their precipitation into the atmosphere (Kubota & Omura, 2017).

We have also shown that the average wave power spectrum of intense H-band EMIC wave packets contains a significant high-frequency tail, reaching ~1.5–3% of their peak power at ω/Ω_{ci} = 0.7–0.9, with a more (less)

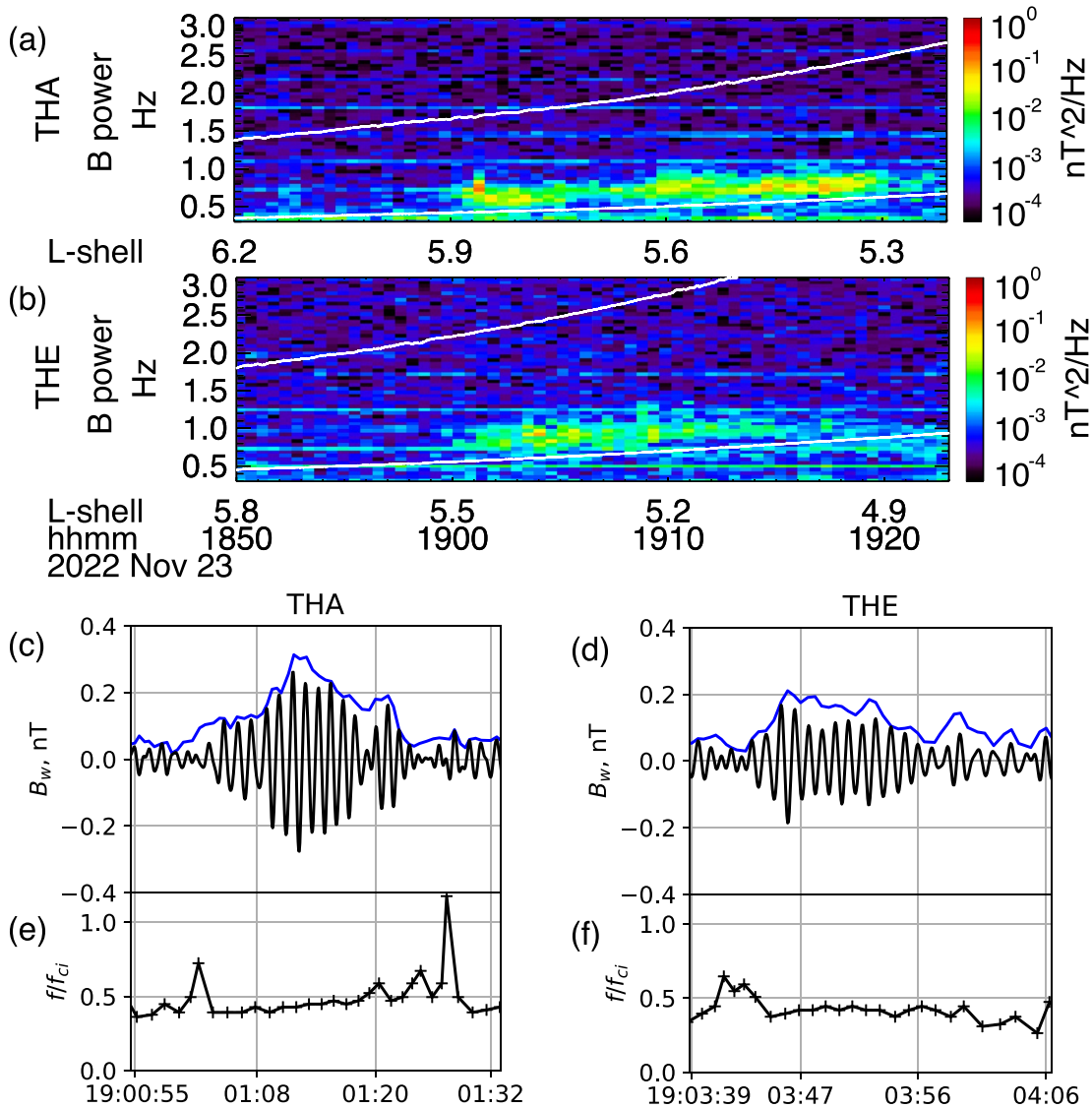

Figure 9. The wave power spectrum of *H* band electromagnetic ion cyclotron waves observed by THEMIS-A and THEMIS-E (a, b). Two white lines from top to bottom indicate the proton and helium cyclotron frequency, respectively. Two examples of wave packets, showing their amplitude and frequency variations, from THEMIS-A and THEMIS-E, respectively (c–f).

substantial high-frequency tail inside the most intense (the shortest) packets and nearly no dependence on the Ω_{pe}/Ω_{ce} range (0–5, 5–15, or > 15). Sub-relativistic (<0.5 MeV) electron precipitation through cyclotron resonance with such waves can occur for $\omega/\Omega_{ci} > 0.7$ and $\Omega_{pe}/\Omega_{ce} > 10$–15. Angelopoulos et al. (2023) have already demonstrated that sub-MeV electron precipitation observed by ELFIN CubeSats in the noon-dusk sector concurrently with stronger EMIC wave-driven >1 MeV precipitation has a spectral shape consistent (down to ~200–300 keV) with quasi-linear resonant scattering by the high-frequency tail of the average H-band EMIC wave power spectrum recorded by the Van Allen Probes in this sector (Zhang et al., 2016). Here, we have further shown that the fraction of EMIC wave power at such high frequencies is much larger within intense packets than in previous global statistics (Zhang et al., 2016) that perform an average over all EMIC waves present within and outside intense packets. The typical amplitudes of such high-frequency waves are ~100 pT. Therefore, our statistical results suggest that quasi-linear resonant interactions with the high-frequency portion of the power spectrum of intense H-band EMIC wave packets, which exhibit strong amplitude modulations, likely provide the main contribution to the sub-relativistic electron precipitation observed during EMIC wave bursts (Capannolo, Li, Ma, Shen, et al., 2019; Capannolo et al., 2023; Hendry et al., 2017, 2019; Zhang, Mourenas, et al., 2021), in agreement with other recent studies (X. An, Artemyev, et al., 2022; Angelopoulos et al., 2023; Denton et al., 2019).

Data Availability Statement

Van Allen Probes wave data is available at https://www.rbsp-ect.lanl.gov/ and https://emfisis.physics.uiowa.edu/data/index. Data was retrieved and analyzed using SPEDAS V4.1, see Angelopoulos et al. (2019). Time History of Events and Macroscale Interactions during Substorms data is available at http://themis.ssl.berkeley.edu.

Acknowledgments
We gratefully acknowledge the Van Allen Probes EMFISIS team for providing the data used in this study. A.V.A., X.-J.Z. acknowledge support by NASA awards 80NSSC23K0403, 80NSSC23K0108, and 80NSSC20K1270, and NSF #2329897. We acknowledge NASA contract NAS5-02099 for the use of data from the THEMIS mission. We thank K. H. Glassmeier, U. Auster, and W. Baumjohann for the use of FGM data provided under the lead of the Technical University of Braunschweig and with financial support through the German Ministry for Economy and Technology and the German Aerospace Center (DLR) under contract 50 OC 0302.

References

Albert, J. M. (2003). Evaluation of quasi-linear diffusion coefficients for EMIC waves in a multispecies plasma. *Journal of Geophysical Research (Space Physics)*, *108*(A6), 1249. https://doi.org/10.1029/2002JA009792

Albert, J. M., Artemyev, A., Li, W., Gan, L., & Ma, Q. (2022). Equations of motion near cyclotron resonance. *Frontiers in Astronomy and Space Sciences*, *9*, 910224. https://doi.org/10.3389/fspas.2022.910224

Albert, J. M., Artemyev, A. V., Li, W., Gan, L., & Ma, Q. (2021). Models of resonant wave-particle interactions. *Journal of Geophysical Research: Space Physics*, *126*(6), e2021JA029216. https://doi.org/10.1029/2021JA029216

Albert, J. M., & Bortnik, J. (2009). Nonlinear interaction of radiation belt electrons with electromagnetic ion cyclotron waves. *Geophysical Research Letters*, *36*(12), 12110. https://doi.org/10.1029/2009GL038904

Albert, J. M., Tao, X., & Bortnik, J. (2013). Aspects of nonlinear wave-particle interactions. In D. Summers, I. U. Mann, D. N. Baker, & M. Schulz (Eds.), *Dynamics of the earth's radiation belts and inner magnetosphere* (p. L12110). https://doi.org/10.1029/2012GM001324

An, X., Artemyev, A., Angelopoulos, V., Zhang, X., Mourenas, D., & Bortnik, J. (2022). Nonresonant scattering of relativistic electrons by electromagnetic ion cyclotron waves in Earth's radiation belts. *Phus. Rev. Lett.*, *129*(13), 135101. https://doi.org/10.1103/PhysRevLett.129.135101

An, X., Artemyev, A., Angelopoulos, V., Zhang, X.-J., Mourenas, D., & Bortnik, J. (2023). Nonresonant scattering of energetic electrons by electromagnetic ion cyclotron waves: Spacecraft observations and theoretical framework. arXiv e-prints, arXiv:2307.03795. https://doi.org/10.48550/arXiv.2307.03795

An, Z., Wu, Y., & Tao, X. (2022). Electron dynamics in a chorus wave field generated from particle-in-cell simulations. *Geophysical Research Letters*, *49*(3), e97778. https://doi.org/10.1029/2022GL097778

Angelopoulos, V. (2008). The THEMIS mission. *Space Science Reviews*, *141*(1–4), 5–34. https://doi.org/10.1007/s11214-008-9336-1

Angelopoulos, V., Cruce, P., Drozdov, A., Grimes, E. W., Hatzigeorgiu, N., King, D. A., et al. (2019). The space physics environment data analysis system (SPEDAS). *Space Science Reviews*, *215*(1), 9. https://doi.org/10.1007/s11214-018-0576-4

Angelopoulos, V., Sibeck, D., Carlson, C. W., McFadden, J. P., Larson, D., Lin, R. P., et al. (2008). First results from the THEMIS mission. *Space Science Reviews*, *141*(1–4), 453–476. https://doi.org/10.1007/s11214-008-9378-4

Angelopoulos, V., Zhang, X. J., Artemyev, A. V., Mourenas, D., Tsai, E., Wilkins, C., et al. (2023). Energetic electron precipitation driven by electromagnetic ion cyclotron waves from ELFIN's low altitude perspective. *Space Science Reviews*, *219*(5), 37. https://doi.org/10.1007/s11214-023-00984-w

Artemyev, A. V., Agapitov, O. V., Mozer, F. S., & Spence, H. (2015). Butterfly pitch angle distribution of relativistic electrons in the outer radiation belt: Evidence of nonadiabatic scattering. *Journal of Geophysical Research*, *120*(6), 4279–4297. https://doi.org/10.1002/2014JA020865

Artemyev, A. V., Neishtadt, A. I., Albert, J. M., Gan, L., Li, W., & Ma, Q. (2021). Theoretical model of the nonlinear resonant interaction of whistler-mode waves and field-aligned electrons. *Physics of Plasmas*, *28*(5), 052902. https://doi.org/10.1063/5.0046635

Artemyev, A. V., Neishtadt, A. I., Vainchtein, D. L., Vasiliev, A. A., Vasko, I. Y., & Zelenyi, L. M. (2018). Trapping (capture) into resonance and scattering on resonance: Summary of results for space plasma systems. *Communications in Nonlinear Science and Numerical Simulations*, *65*, 111–160. https://doi.org/10.1016/j.cnsns.2018.05.004

Auster, H. U., Glassmeier, K. H., Magnes, W., Aydogar, O., Baumjohann, W., Constantinescu, D., et al. (2008). The THEMIS fluxgate magnetometer. *Space Science Reviews*, *141*(1–4), 235–264. https://doi.org/10.1007/s11214-008-9365-9

Bashir, M. F., Artemyev, A., Zhang, X.-J., & Angelopoulos, V. (2022). Hot plasma effects on electron resonant scattering by electromagnetic ion cyclotron waves. *Geophysical Research Letters*, *49*(11), e99229. https://doi.org/10.1029/2022GL099229

Birmingham, T. J. (1984). Pitch angle diffusion in the Jovian magnetodisc. *Journal of Geophysical Research*, *89*(A5), 2699–2707. https://doi.org/10.1029/JA089iA05p02699

Blum, L. W., Agapitov, O., Bonnell, J. W., Kletzing, C., & Wygant, J. (2016). EMIC wave spatial and coherence scales as determined from multipoint Van Allen Probe measurements. *Geophysical Research Letters*, *43*(10), 4799–4807. https://doi.org/10.1002/2016GL068799

Blum, L. W., Bonnell, J. W., Agapitov, O., Paulson, K., & Kletzing, C. (2017). EMIC wave scale size in the inner magnetosphere: Observations from the dual Van Allen Probes. *Geophysical Research Letters*, *44*(3), 1227–1233. https://doi.org/10.1002/2016GL072316

Bortnik, J., Albert, J. M., Artemyev, A., Li, W., Jun, C.-W., Grach, V. S., & Demekhov, A. G. (2022). Amplitude dependence of nonlinear precipitation blocking of relativistic electrons by large amplitude EMIC waves. *Geophysical Research Letters*, *49*(12), e98365. https://doi.org/10.1029/2022GL098365

Buchner, J., & Zelenyi, L. V. (1989). Regular and chaotic charged particle motion in magnetotaillike field reversals: 1. Basic theory of trapped motion. *Journal of Geophysical Research*, *94*(A9), 11821–11842. https://doi.org/10.1029/JA094iA09p11821

Cao, J., Shprits, Y. Y., Ni, B., & Zhelavskaya, I. S. (2017). Scattering of ultra-relativistic electrons in the Van Allen radiation belts accounting for hot plasma effects. *Scientific Reports*, *7*(1), 17719. https://doi.org/10.1038/s41598-017-17739-7

Capannolo, L., Li, W., Ma, Q., Chen, L., Shen, X. C., Spence, H. E., et al. (2019). Direct observation of subrelativistic electron precipitation potentially driven by EMIC waves. *Geophysical Research Letters*, *46*(22), 12711–12721. https://doi.org/10.1029/2019GL084202

Capannolo, L., Li, W., Ma, Q., Qin, M., Shen, X. C., Angelopoulos, V., et al. (2023). Electron precipitation observed by elfin using proton precipitation as a proxy for electromagnetic ion cyclotron (emic) waves. *Geophysical Research Letters*, *50*(21), e2023GL103519. https://doi.org/10.1029/2023GL103519

Capannolo, L., Li, W., Ma, Q., Shen, X. C., Zhang, X. J., Redmon, R. J., et al. (2019). Energetic electron precipitation: Multievent analysis of its spatial extent during EMIC wave activity. *Journal of Geophysical Research (Space Physics)*, *124*(4), 2466–2483. https://doi.org/10.1029/2018JA026291

Chen, L., Thorne, R. M., Bortnik, J., & Zhang, X.-J. (2016). Nonresonant interactions of electromagnetic ion cyclotron waves with relativistic electrons. *Journal of Geophysical Research*, *121*(10), 9913–9925. https://doi.org/10.1002/2016JA022813

Chen, L., Zhu, H., & Zhang, X. (2019). Wavenumber analysis of EMIC waves. *Geophysical Research Letters*, *46*(11), 5689–5697. https://doi.org/10.1029/2019GL082686

Chirikov, B. V. (1987). *Particle dynamics in magnetic traps* (1st ed., Vol. 13). Consultants Bureau.

Delcourt, D. C., Martin, R. F., Jr., & Alem, F. (1994). A simple model of magnetic moment scattering in a field reversal. *Geophysical Research Letters*, *21*(14), 1543–1546. https://doi.org/10.1029/94GL01291

Denton, R. E., Ofman, L., Shprits, Y. Y., Bortnik, J., Millan, R. M., Rodger, C. J., et al. (2019). Pitch angle scattering of sub-MeV relativistic electrons by electromagnetic ion cyclotron waves. *Journal of Geophysical Research (Space Physics)*, *124*(7), 5610–5626. https://doi.org/10.1029/2018JA026384

Drozdov, A. Y., Shprits, Y. Y., Usanova, M. E., Aseev, N. A., Kellerman, A. C., & Zhu, H. (2017). EMIC wave parameterization in the long-term VERB code simulation. *Journal of Geophysical Research*, *122*(8), 8488–8501. https://doi.org/10.1002/2017JA024389

Grach, V. S., Artemyev, A. V., Demekhov, A. G., Zhang, X.-J., Bortnik, J., Angelopoulos, V., et al. (2022). Relativistic electron precipitation by EMIC waves: Importance of nonlinear resonant effects. *Geophysical Research Letters*, *49*(17), e99994. https://doi.org/10.1029/2022GL099994

Grach, V. S., & Demekhov, A. G. (2018a). Resonance interaction of relativistic electrons with ion-cyclotron waves. I. Specific features of the nonlinear interaction regimes. *Radiophysics and Quantum Electronics*, *60*(12), 942–959. https://doi.org/10.1007/s11141-018-9860-0

Grach, V. S., & Demekhov, A. G. (2018b). Resonant interaction of relativistic electrons with electromagnetic ion-cyclotron waves. II. Integral parameters of interaction regimes. *Radiophysics and Quantum Electronics*, *61*(6), 389–401. https://doi.org/10.1007/s11141-018-9900-9

Grach, V. S., & Demekhov, A. G. (2020). Precipitation of relativistic electrons under resonant interaction with electromagnetic ion cyclotron wave packets. *Journal of Geophysical Research (Space Physics)*, *125*(2), e27358. https://doi.org/10.1029/2019JA027358

Grach, V. S., Demekhov, A. G., & Larchenko, A. V. (2021). Resonant interaction of relativistic electrons with realistic electromagnetic ion-cyclotron wave packets. *Earth Planets and Space*, *73*(1), 129. https://doi.org/10.1186/s40623-021-01453-w

Hanzelka, M., Li, W., & Ma, Q. (2023). Parametric analysis of pitch angle scattering and losses of relativistic electrons by oblique EMIC waves. *Frontiers in Astronomy and Space Sciences*, *10*, 1163515. https://doi.org/10.3389/fspas.2023.1163515

Hanzelka, M., Li, W., Ma, Q., Qin, M., Shen, X.-C., Capannolo, L., & Gan, L. (2023). Full-wave modeling of emic wave packets: Ducted propagation and reflected waves. *Frontiers in Astronomy and Space Sciences*, *10*, 1251563. https://doi.org/10.3389/fspas.2023.1251563

Hendry, A. T., Rodger, C. J., & Clilverd, M. A. (2017). Evidence of sub-MeV EMIC-driven electron precipitation. *Geophysical Research Letters*, *44*(3), 1210–1218. https://doi.org/10.1002/2016GL071807

Hendry, A. T., Santolik, O., Kletzing, C. A., Rodger, C. J., Shiokawa, K., & Baishev, D. (2019). Multi-instrument observation of nonlinear EMIC-driven electron precipitation at sub-MeV energies. *Geophysical Research Letters*, *46*(13), 7248–7257. https://doi.org/10.1029/2019GL082401

Jun, C.-W., Miyoshi, Y., Kurita, S., Yue, C., Bortnik, J., Lyons, L., et al. (2021). The characteristics of EMIC waves in the magnetosphere based on the Van Allen probes and arase observations. *Journal of Geophysical Research (Space Physics)*, *126*(6), e29001. https://doi.org/10.1029/2020JA029001

Jun, C. W., Yue, C., Bortnik, J., Lyons, L. R., Nishimura, Y., & Kletzing, C. (2019). EMIC wave properties associated with and without injections in the inner magnetosphere. *Journal of Geophysical Research (Space Physics)*, *124*(3), 2029–2045. https://doi.org/10.1029/2018JA026279

Kersten, T., Horne, R. B., Glauert, S. A., Meredith, N. P., Fraser, B. J., & Grew, R. S. (2014). Electron losses from the radiation belts caused by EMIC waves. *Journal of Geophysical Research*, *119*(11), 8820–8837. https://doi.org/10.1002/2014JA020366

Kim, E.-H., & Johnson, J. R. (2016). Full-wave modeling of emic waves near the he+ gyrofrequency. *Geophysical Research Letters*, *43*(1), 13–21. https://doi.org/10.1002/2015GL066978

Kletzing, C. A., Kurth, W. S., Acuna, M., MacDowall, R. J., Torbert, R. B., Averkamp, T., et al. (2013). The electric and magnetic field instrument suite and integrated science (EMFISIS) on RBSP. *Space Science Reviews*, *179*(1–4), 127–181. https://doi.org/10.1007/s11214-013-9993-6

Kubota, Y., & Omura, Y. (2017). Rapid precipitation of radiation belt electrons induced by EMIC rising tone emissions localized in longitude inside and outside the plasmapause. *Journal of Geophysical Research (Space Physics)*, *122*(1), 293–309. https://doi.org/10.1002/2016JA023267

Kubota, Y., Omura, Y., & Summers, D. (2015). Relativistic electron precipitation induced by EMIC-triggered emissions in a dipole magnetosphere. *Journal of Geophysical Research (Space Physics)*, *120*(6), 4384–4399. https://doi.org/10.1002/2015JA021017

Kurth, W. S., De Pascuale, S., Faden, J. B., Kletzing, C. A., Hospodarsky, G. B., Thaller, S., & Wygant, J. R. (2015). Electron densities inferred from plasma wave spectra obtained by the Waves instrument on Van Allen Probes. *Journal of Geophysical Research*, *120*(2), 904–914. https://doi.org/10.1002/2014JA020857

Liu, S., Zhang, J., Chen, L., Zhu, H., & He, Z. (2018). Examining wave vector and minimum cyclotron resonant electron energy of EMIC waves with magnetospheric multiscale mission. *Geophysical Research Letters*, *45*(19), 10138–10149. https://doi.org/10.1029/2018GL079737

Mauk, B. H., Fox, N. J., Kanekal, S. G., Kessel, R. L., Sibeck, D. G., & Ukhorskiy, A. (2013). Science objectives and rationale for the radiation belt storm probes mission. *Space Science Reviews*, *179*(1–4), 3–27. https://doi.org/10.1007/s11214-012-9908-y

Meredith, N. P., Horne, R. B., Kersten, T., Fraser, B. J., & Grew, R. S. (2014). Global morphology and spectral properties of EMIC waves derived from CRRES observations. *Journal of Geophysical Research*, *119*(7), 5328–5342. https://doi.org/10.1002/2014JA020064

Millan, R. M., & Thorne, R. M. (2007). Review of radiation belt relativistic electron losses. *Journal of Atmospheric and Solar-Terrestrial Physics*, *69*(3), 362–377. https://doi.org/10.1016/j.jastp.2006.06.019

Mourenas, D., Zhang, X.-J., Artemyev, A. V., Angelopoulos, V., Thorne, R. M., Bortnik, J., et al. (2018). Electron nonlinear resonant interaction with short and intense parallel Chorus wave packets. *Journal of Geophysical Research*, *123*(6), 4979–4999. https://doi.org/10.1029/2018JA025417

Mourenas, D., Zhang, X. J., Nunn, D., Artemyev, A. V., Angelopoulos, V., Tsai, E., & Wilkins, C. (2022). Short Chorus wave packets: Generation within chorus elements, statistics, and consequences on energetic electron precipitation. *Journal of Geophysical Research (Space Physics)*, *127*(5), e30310. https://doi.org/10.1029/2022JA030310

Nakamura, S., Omura, Y., Kletzing, C., & Baker, D. N. (2019). Rapid precipitation of relativistic electron by EMIC rising-tone emissions observed by the Van Allen probes. *Journal of Geophysical Research (Space Physics)*, *124*(8), 6701–6714. https://doi.org/10.1029/2019JA026772

Nakamura, S., Omura, Y., Shoji, M., Nosé, M., Summers, D., & Angelopoulos, V. (2015). Subpacket structures in EMIC rising tone emissions observed by the THEMIS probes. *Journal of Geophysical Research*, *120*(9), 7318–7330. https://doi.org/10.1002/2014JA020764

Neishtadt, A. I. (2000). On the accuracy of persistence of adiabatic invariant in single-frequency system. *Regular & Chaotic Dynamics*, *5*(2), 213–218. https://doi.org/10.1070/RD2000v005n02ABEH000143

Ni, B., Cao, X., Zou, Z., Zhou, C., Gu, X., Bortnik, J., et al. (2015). Resonant scattering of outer zone relativistic electrons by multiband EMIC waves and resultant electron loss time scales. *Journal of Geophysical Research*, *120*(9), 7357–7373. https://doi.org/10.1002/2015JA021466

Nunn, D., Zhang, X. J., Mourenas, D., & Artemyev, A. V. (2021). Generation of realistic short chorus wave packets. *Geophysical Research Letters*, *48*(7), e92178. https://doi.org/10.1029/2020GL092178

Omura, Y., Matsumoto, H., Nunn, D., & Rycroft, M. J. (1991). A review of observational, theoretical and numerical studies of VLF triggered emissions. *Journal of Atmospheric and Terrestrial Physics*, *53*(5), 351–368. https://doi.org/10.1016/0021-9169(91)90031-2

Omura, Y., Pickett, J., Grison, B., Santolik, O., Dandouras, I., Engebretson, M., et al. (2010). Theory and observation of electromagnetic ion cyclotron triggered emissions in the magnetosphere. *Journal of Geophysical Research*, *115*(A7), A07234. https://doi.org/10.1029/2010JA015300

Omura, Y., & Zhao, Q. (2012). Nonlinear pitch angle scattering of relativistic electrons by EMIC waves in the inner magnetosphere. *Journal of Geophysical Research*, *117*(A8), 8227. https://doi.org/10.1029/2012JA017943

Omura, Y., & Zhao, Q. (2013). Relativistic electron microbursts due to nonlinear pitch angle scattering by EMIC triggered emissions. *Journal of Geophysical Research*, *118*(8), 5008–5020. https://doi.org/10.1002/jgra.50477

Ross, J. P. J., Glauert, S. A., Horne, R. B., Watt, C. E., Meredith, N. P., & Woodfield, E. E. (2020). A new approach to constructing models of electron diffusion by EMIC waves in the radiation belts. *Geophysical Research Letters*, *47*(20), e88976. https://doi.org/10.1029/2020GL088976

Ross, J. P. J., Glauert, S. A., Horne, R. B., Watt, C. E. J., & Meredith, N. P. (2021). On the variability of EMIC waves and the consequences for the relativistic electron radiation belt population. *Journal of Geophysical Research (Space Physics)*, *126*(12), e29754. https://doi.org/10.1029/2021JA029754

Sagdeev, R. Z., & Shafranov, V. D. (1961). On the instability of a plasma with an anisotropic distribution of velocities in a magnetic field. *Soviet Phys. JETP*, *12*(1), 130–132.

Shklyar, D. R., & Matsumoto, H. (2009). Oblique whistler-mode waves in the inhomogeneous magnetospheric plasma: Resonant interactions with energetic charged particles. *Surveys in Geophysics*, *30*(2), 55–104. https://doi.org/10.1007/s10712-009-9061-7

Shoji, M., Miyoshi, Y., Omura, Y., Kistler, L., Kasaba, Y., Matsuda, S., et al. (2018). Instantaneous frequency analysis on nonlinear EMIC emissions: Arase observation. *Geophysical Research Letters*, *45*(24), 13199–13205. https://doi.org/10.1029/2018GL079765

Shoji, M., & Omura, Y. (2013). Triggering process of electromagnetic ion cyclotron rising tone emissions in the inner magnetosphere. *Journal of Geophysical Research*, *118*(9), 5553–5561. https://doi.org/10.1002/jgra.50523

Shprits, Y. Y., Drozdov, A. Y., Spasojevic, M., Kellerman, A. C., Usanova, M. E., Engebretson, M. J., et al. (2016). Wave-induced loss of ultra-relativistic electrons in the Van Allen radiation belts. *Nature Communications*, *7*(1), 12883. https://doi.org/10.1038/ncomms12883

Shprits, Y. Y., Subbotin, D. A., Meredith, N. P., & Elkington, S. R. (2008). Review of modeling of losses and sources of relativistic electrons in the outer radiation belt II: Local acceleration and loss. *Journal of Atmospheric and Solar-Terrestrial Physics*, *70*(14), 1694–1713. https://doi.org/10.1016/j.jastp.2008.06.014

Silin, I., Mann, I. R., Sydora, R. D., Summers, D., & Mace, R. L. (2011). Warm plasma effects on electromagnetic ion cyclotron wave MeV electron interactions in the magnetosphere. *Journal of Geophysical Research (Space Physics)*, *116*(A5), A05215. https://doi.org/10.1029/2010JA016398

Su, Z., Zhu, H., Xiao, F., Zheng, H., Shen, C., Wang, Y., & Wang, S. (2012). Bounce-averaged advection and diffusion coefficients for monochromatic electromagnetic ion cyclotron wave: Comparison between test-particle and quasi-linear models. *Journal of Geophysical Research (Space Physics)*, *117*(A9), A09222. https://doi.org/10.1029/2012JA017917

Summers, D., & Thorne, R. M. (2003). Relativistic electron pitch-angle scattering by electromagnetic ion cyclotron waves during geomagnetic storms. *Journal of Geophysical Research*, *108*(A4), 1143. https://doi.org/10.1029/2002JA009489

Tao, X., Bortnik, J., Albert, J. M., Thorne, R. M., & Li, W. (2013). The importance of amplitude modulation in nonlinear interactions between electrons and large amplitude whistler waves. *Journal of Atmospheric and Solar-Terrestrial Physics*, *99*, 67–72. https://doi.org/10.1016/j.jastp.2012.05.012

Tao, X., Zonca, F., & Chen, L. (2017). Identify the nonlinear wave-particle interaction regime in rising tone chorus generation. *Geophysical Research Letters*, *44*(8), 3441–3446. https://doi.org/10.1002/2017GL072624

Teng, S., Tao, X., Xie, Y., Zonca, F., Chen, L., Fang, W. B., & Wang, S. (2017). Analysis of the duration of rising tone chorus elements. *Geophysical Research Letters*, *44*(24), 12074–12082. https://doi.org/10.1002/2017GL075824

Thorne, R. M., & Kennel, C. F. (1971). Relativistic electron precipitation during magnetic storm main phase. *Journal of Geophysical Research*, *76*(19), 4446–4453. https://doi.org/10.1029/JA076i019p04446

Usanova, M. E. (2021). Energy exchange between electromagnetic ion cyclotron (EMIC) waves and thermal plasma: From theory to observations. *Frontiers in Astronomy and Space Sciences*, *8*, 150. https://doi.org/10.3389/fspas.2021.744344

Usanova, M. E., Mann, I. R., Bortnik, J., Shao, L., & Angelopoulos, V. (2012). THEMIS observations of electromagnetic ion cyclotron wave occurrence: Dependence on AE, SYMH, and solar wind dynamic pressure. *Journal of Geophysical Research*, *117*(A10), 10218. https://doi.org/10.1029/2012JA018049

Usanova, M. E., Mann, I. R., Kale, Z. C., Rae, I. J., Sydora, R. D., Sandanger, M., et al. (2010). Conjugate ground and multisatellite observations of compression-related EMIC Pc1 waves and associated proton precipitation. *Journal of Geophysical Research (Space Physics)*, *115*(A7), A07208. https://doi.org/10.1029/2009JA014935

Wang, Z., Zhang, L., & Zhong, J. (2023). The electromagnetic ion cyclotron instability affected by the temperature anisotropic electrons in the inner magnetosphere. *Geophysical Research Letters*, *50*(22), e2023GL105876. https://doi.org/10.1029/2023GL105876

Wygant, J. R., Bonnell, J. W., Goetz, K., Ergun, R. E., Mozer, F. S., Bale, S. D., et al. (2013). The electric field and waves instruments on the radiation belt storm probes mission. *Space Science Reviews*, *179*(1–4), 183–220. https://doi.org/10.1007/s11214-013-0013-7

Xu, Y., & Egedal, J. (2022). Pitch angle scattering of fast particles by low frequency magnetic fluctuations. *Physics of Plasmas*, *29*(1), 010701. https://doi.org/10.1063/5.0077787

Zhang, X. J., Agapitov, O., Artemyev, A. V., Mourenas, D., Angelopoulos, V., Kurth, W. S., et al. (2020). Phase decoherence within intense chorus wave packets constrains the efficiency of nonlinear resonant electron acceleration. *Geophysical Research Letters*, *47*(20), e89807. https://doi.org/10.1029/2020GL089807

Zhang, X.-J., Angelopoulos, V., Artemyev, A., Mourenas, D., Agapitov, O., Tsai, E., & Wilkins, C. (2023). Temporal scales of electron precipitation driven by whistler-mode waves. *Journal of Geophysical Research (Space Physics)*, *128*(1), e2022JA031087. https://doi.org/10.1029/2022JA031087

Zhang, X. J., Demekhov, A. G., Katoh, Y., Nunn, D., Tao, X., Mourenas, D., et al. (2021). Fine structure of chorus wave packets: Comparison between observations and wave generation models. *Journal of Geophysical Research (Space Physics)*, *126*(8), e29330. https://doi.org/10.1029/2021JA029330

Zhang, X.-J., Li, W., Thorne, R. M., Angelopoulos, V., Bortnik, J., Kletzing, C. A., et al. (2016). Statistical distribution of EMIC wave spectra: Observations from van Allen Probes. *Geophysical Research Letters*, *43*(24), 12. https://doi.org/10.1002/2016GL071158

Zhang, X. J., Mourenas, D., Artemyev, A. V., Angelopoulos, V., Kurth, W. S., Kletzing, C. A., & Hospodarsky, G. B. (2020). Rapid frequency variations within intense chorus wave packets. *Geophysical Research Letters*, *47*(15), e88853. https://doi.org/10.1029/2020GL088853

Zhang, X. J., Mourenas, D., Shen, X. C., Qin, M., Artemyev, A. V., Ma, Q., et al. (2021). Dependence of relativistic electron precipitation in the ionosphere on EMIC wave minimum resonant energy at the conjugate equator. *Journal of Geophysical Research (Space Physics)*, *126*(5), e29193. https://doi.org/10.1029/2021JA029193